



# Disentangling the Components of the Milky Way

INFERRING THE STRUCTURE OF THE MILKY WAY IN PHASE-SPACE USING  
GAUSSIAN MIXTURE MODELLING WITH EXTREME DECONVOLUTION

A REPORT PRESENTED

BY

RAUNAQ SINGH RAI

## Departments

Department of Physics (Cavendish Laboratory)  
Institute of Astronomy

## Degree

MPhil in Data Intensive Science

## Supervision

Dr Anke Arentsen



St Edmund's College  
University of Cambridge

29th June 2025

## Abstract

The Milky Way Galaxy is a complex system composed of multiple stellar components, each with distinct chemical and kinematic properties. The presence of a very-metal-poor disk structure has been speculated, which would challenge the conventional view that the disk formed later from already enriched gas. By reproducing and extending the Extreme-Deconvolution Gaussian Mixture Model (XD-GMM) study of [Zhang et al. \[2024\]](#), we investigate the presence of a very-metal-poor disk in the Milky Way using data catalogues from [Andrae et al. \[2023\]](#), [Li et al. \[2023\]](#) and [Bailer-Jones et al. \[2021\]](#).

In general, our results are in agreement with that of [Zhang et al. \[2024\]](#): below  $[M/H] \simeq -1.6$  we do not find evidence for a coherent, rotationally supported disk component. The prograde rotation signal stems from a prograde halo with a net prograde rotation of  $v_\phi \simeq 68 \text{ km s}^{-1}$ . In this regime, no component satisfies  $v_\phi/\sigma_\phi > 1$ ; any thick-disk contribution in the very-metal-poor interval  $-3.0 < [M/H] < -1.6$  is therefore negligible.

Splitting the sample by  $\alpha$  abundance sharpens the timeline of disk growth. Building on [Viswanathan et al. \[2024\]](#) with the extreme-deconvolution framework of [Zhang et al. \[2024\]](#), we show that a rotation-supported thick disk appears in the *high- $\alpha$*  branch at  $[M/H] \gtrsim -1.6$ , whereas *low- $\alpha$*  stars remain halo-dominated until a rapid spin-up at  $[M/H] \approx -1.3$ , which marks the thin-disk birth. These metallicity- $\alpha$  thresholds ( $-1.6$  dex and  $-1.3$  dex) constitute hard priors for chemo-dynamical simulations, a clean survey filter for WEAVE, 4MOST and SDSS-V to isolate the oldest disk stars, and inputs for AURIGA and FIRE-2 zoom suites to generate testable JWST and Rubin-LSST predictions for disk structure in other spiral galaxies.

**Word count: 6947**

## List of Figures

1	Properties of the final RGB sample after all quality and footprint cuts. <i>Left</i> : heliocentric-distance histogram for the whole sample (grey); the subsets with $-3 < [\text{M}/\text{H}] < -1$ and $-3 < [\text{M}/\text{H}] < -2$ are shown in solid red and dashed blue, respectively. <i>Middle</i> : density map in Galactocentric cylindrical coordinates. The empty band at low $ Z $ is a selection artefact of our latitude/extinction cuts, which deliberately remove the thin-disk mid-plane; the concentration around $R \simeq 5\text{--}8 \text{ kpc}$ reflects the volume accessible to bright RGB stars interior to the Solar circle and coincides with the molecular ring region where the stellar surface density peaks. <i>Right</i> : Metallicity distribution of our data sample. Line colours are the same as in the left panel. (A reproduction of Figure 1 from Zhang et al. [2024]) . . . . .	9
2	Column-normalised density in the $v_\phi$ –[M/H] plane. <i>Left</i> : the bright-RGB catalogue of Andrae et al. [2023]. <i>Right</i> : the same sample after all distance, dust, and quality cuts. Greyscale pixels show the normalised counts in each metallicity bin; the red dashed curve is the median $v_\phi$ , and the black curves trace the 16 <sup>th</sup> and 84 <sup>th</sup> percentiles. (A reproduction of Figure 2 from Zhang et al. [2024]) . . . . .	10
3	Galactocentric velocity distributions as a function of metallicity. Each panel shows the column-normalised density of stars in the $v_R$ – $v_\phi$ plane for the metallicity interval printed at the top.(A reproduction of Figure 3 from Zhang et al. [2024]) . . . . .	10
4	Ellipses mark the approximate extent of the thin disk (black), thick disk (gray), GS/E debris (pink) and the pressure-supported stellar halo (purple). The figure should be used as a visual key for interpreting the data panels in Fig. 3. . . . .	11
5	BIC distributions as a function of the number of GMM components in each metallicity bin. The optimum number of components is indicated by the minimum BIC value (highlighted in red). (A reproduction of Figure 4 from Zhang et al. [2024]) . . . . .	12
6	Gaussian Mixture Model decompositions of the stellar velocity distribution in the $v_R$ – $v_\phi$ plane for each metallicity bin. The lower panels show the 2D $v_R$ – $v_\phi$ distributions with GMM components overplotted as $1\sigma$ ellipses, and the upper panels display each component’s fractional contribution. (Reproduced from Zhang et al. 2024 Figure 5.) Links to the fully interactive 3-D plots for each bin are provided as hyperlinks in the subcaptions. . . . .	13
7	Ratio of mean rotational velocity to azimuthal velocity dispersion, $V_{\text{rot}}/\sigma_\phi$ , for individual GMM components in each metallicity bin. Larger circles correspond to more dominant components. Colours match the GMM components in Figure 6.(A reproduction of Figure 6 from Zhang et al. [2024]) . . . . .	15
8	Top: Normalised residual maps between observed and GMM-predicted velocity distributions in $(v_R, v_\phi)$ for the VMP (left) and IMP (right) metallicity bins. Grey ellipses show the $2\sigma$ contour of the fiducial thick disk model. Bottom: Disk residuals as a function of injected disk fraction. The dashed line and blue band indicate the observed residual and its uncertainty. The solid black line and red region show mock test results and their uncertainties. (A reproduction of Figure 7 from Zhang et al. [2024]) . . . . .	17

9	Density of stars in the $[\alpha/\text{M}]$ – $[\text{M}/\text{H}]$ plane. The high- $\alpha$ and low- $\alpha$ sequences are separated by the piecewise linear boundary described in the text. The transition zone between the two sequences is clearly removed from this plot and discarded from subsequent analysis. (A reproduction of Figure 1 in Viswanathan et al. [2024]) . . . . .	19
10	Mean $[\text{M}/\text{H}]$ colour-coded in the Galactocentric $R$ – $z$ plane. <i>Top</i> : the complete $G < 16$ RGB sample. <i>Bottom left</i> : high- $\alpha$ stars; <i>bottom right</i> : low- $\alpha$ stars. The high- $\alpha$ population is more centrally concentrated and shows a shallower vertical metallicity gradient. (A reproduction of Figure 2 in Viswanathan et al. [2024]) . . . . .	20
11	Azimuthal velocity versus metallicity. Left: full RGB sample. Centre: high- $\alpha$ stars. Right: low- $\alpha$ stars. Contours show running medians (red) and the 16th/84th percentiles (black). (Adapted from Fig. 3 of Viswanathan et al. 2024.) . . . . .	21
12	BIC scores for different metallicity bins, grouped by high- and low- $\alpha$ populations. . . . .	22
13	XD–GMM decomposition of high- $\alpha$ giants in four metallicity bins. Grey ellipses mark the $1\sigma$ contours of each Gaussian component; click the subcaptions to open the interactive 3D plots. . . . .	22
14	XD–GMM decomposition of low- $\alpha$ giants in four metallicity bins. Grey ellipses show the $1\sigma$ contours of every Gaussian component; click the subcaptions to open the interactive 3D plots. . . . .	23
15	Ratio of the mean rotational velocity to azimuthal velocity dispersion, $V_{\text{rot}}/\sigma_\phi$ , for individual GMM components in each metallicity bin. Larger circles represent more dominant components. Colours correspond to those in Figures 13 and 14. This is created in the same way as Figure 7. . . . .	24

## List of Tables

1	Parameters of the Gaussian mixture model fittings in different metallicity bins. The unit for all velocity columns is $\text{km s}^{-1}$ . . . . .	14
2	Number of Gaussian Mixture components selected by the BIC for each metallicity bin, split by $\alpha$ -sequence. . . . .	21
3	GMM component weights and kinematics for the high- $\alpha$ sequence. Velocities are in $\text{km s}^{-1}$ . Weights indicate the fraction of stars per metallicity bin. . . . .	23
4	XD-GMM component weights and kinematics for the low- $\alpha$ sequence. Veloc- ities are in $\text{km s}^{-1}$ . Weights are the fractional contribution of each component. .	24

# Contents

<b>1</b>	<b>Introduction</b>	<b>6</b>
1.1	Components of the Milky Way . . . . .	6
1.2	Metallicity as a Cosmic Clock . . . . .	6
1.3	Accreted Halo and Metal-poor Disk Origins . . . . .	7
1.4	This Work . . . . .	7
<b>2</b>	<b>Data</b>	<b>8</b>
2.1	Sample construction . . . . .	8
2.2	Galactocentric Positions and Velocities . . . . .	9
<b>3</b>	<b>Methodology</b>	<b>11</b>
3.1	Gaussian Mixture Model . . . . .	11
3.2	Number of Gaussian Components . . . . .	12
<b>4</b>	<b>Results</b>	<b>13</b>
4.1	Gaussian Mixture Model Fit . . . . .	13
4.2	Rotational Support and the Onset of Disk Formation . . . . .	14
4.3	Residual Analysis for Hidden Disk Populations . . . . .	16
<b>5</b>	<b>Extension Analysis</b>	<b>17</b>
5.1	Alpha–Element Abundance . . . . .	17
5.2	Data . . . . .	18
5.3	Gaussian Mixture Model Fit . . . . .	21
5.4	High alpha Gaussian Mixture Model Fit . . . . .	22
5.5	Low alpha Gaussian Mixture Model Fit . . . . .	23
5.6	Contrasting the high and low $\alpha$ GMMs . . . . .	24
<b>6</b>	<b>Discussion</b>	<b>25</b>
6.1	Reproducability of Zhang et al. [2024] . . . . .	25
6.2	Expansion of Viswanathan et al. [2024] . . . . .	26
6.3	Selection Effects . . . . .	26
6.4	Limitations of GMM . . . . .	27
6.5	Recommendations and Next Steps . . . . .	27
<b>7</b>	<b>Conclusion</b>	<b>28</b>

# 1 Introduction

The Milky Way Galaxy, host to our solar system, is a spiral galaxy with a centre located approximately 150 000 trillion miles from Earth. Its formation history is complex and remains an active area of research. Being embedded within the Milky Way means we can study it in greater detail than any external galaxy, testing models of galaxy formation with high-precision observational data. One of the central aims of Galactic Archaeology is to reconstruct the Milky Way’s assembly by examining the chemical compositions and dynamical properties of its stars.

In this project, we reproduce and extend the analysis of [Zhang et al. \[2024\]](#), who investigated a very metal-poor disk component in the Milky Way. Very metal poor stars, formed from an interstellar medium unpolluted by earlier generations of supernovae, are among the oldest relics in the Galaxy. Discovering them on disk-like orbits would challenge the conventional view that the disk formed later from already enriched gas [[Bland-Hawthorn and Gerhard, 2016](#)], implying instead an earlier onset of disk assembly.

## 1.1 Components of the Milky Way

The Milky Way is commonly decomposed into four stellar components: a *thin disk*, a *thick disk*, a central *bulge/bar*, and a roughly spherical *halo* [[Bland-Hawthorn and Gerhard, 2016](#), [Helmi, 2020](#)]. The thin disk describes the majority of stars and most of the interstellar gas in the galaxy. Ongoing star formation is concentrated in the “molecular–gas ring” where young, metal-rich stars trace nearly circular, co-rotating orbits with low velocity dispersion ( $\sigma_\phi \simeq 20 \text{ km s}^{-1}$ ). Above the mid-plane lies the thick disk: an older ( $\gtrsim 8\text{--}10 \text{ Gyr}$ ), moderately metal-poor population , a scale height of  $z_{\text{scale}} \approx 1 \text{ kpc}$ , and hotter kinematics ( $\sigma_z \simeq 40 \text{ km s}^{-1}$ ) while still retaining net prograde rotation. Inside  $R \lesssim 2 \text{ kpc}$ , the central bulge (partly bar-shaped) hosts both old, metal-rich stars and a younger, actively forming component; stellar motions there combine bar-driven streaming with high random velocities ( $\sigma \sim 100 \text{ km s}^{-1}$ ). Encasing all of these is the stellar halo, which contributes only a few per cent of the total stellar mass yet includes the Galaxy’s oldest, most metal-poor stars ( $[\text{Fe}/\text{H}] \lesssim -1.5$ ) on highly eccentric or even retrograde orbits. Its low density, rich substructure, and kinematics indicate an origin in the hierarchical accretion and tidal disruption of dwarf galaxies and globular clusters. The spatial distribution, chemistry, and dynamics of these four components supply clues to the Milky Way’s formation history and its sequence of merger events.

## 1.2 Metallicity as a Cosmic Clock

Precise ages for individual old stars are difficult to measure, so their chemical composition, most commonly the iron-to-hydrogen ratio  $[\text{Fe}/\text{H}]$ , is used as a surrogate clock. Very metal-poor (VMP) stars must have formed before successive generations of Type II and Type Ia supernovae had substantially enriched the interstellar medium, and therefore have low  $[\text{Fe}/\text{H}]$  values. Metallicity is inferred spectroscopically by measuring the equivalent widths of metal absorption lines, particularly Fe I and the Ca II H and K lines at 396.8 nm and 393.4 nm, respectively. After correcting for stellar effective temperature and surface gravity, the relative strengths of these lines yield elemental abundances [[Gray, 2005](#)]. Large surveys (for example APOGEE, GALAH, LAMOST, and the Gaia XP spectra) now provide such measurements for millions of stars, enabling empirical age–metallicity relations that link chemistry to stellar chronometry [e.g. [Nordström et al., 2004](#), [Haywood et al., 2013](#), [Leung and Bovy, 2019](#), [Anders et al., 2023](#)]. These studies consistently show that stars with  $[\text{Fe}/\text{H}] \lesssim -1$  are typically

older than  $\sim 10$  Gyr, making low-metallicity populations valuable probes of the Milky Way's earliest epochs.

### 1.3 Accreted Halo and Metal-poor Disk Origins

Chemical and kinematic evidence confirms that the stellar halo is largely of accreted origin. In the  $\Lambda$ CDM framework, Milky Way mass haloes assemble hierarchically, undergoing numerous minor mergers and a few major ones [Springel et al., 2008]. While hundreds of subhaloes are accreted over cosmic time, only a small fraction form stars: below a virial mass of  $\sim 10^{11} M_\odot$ , reionisation and feedback suppress star formation [Purcell et al., 2007, Bullock and Boylan-Kolchin, 2017]. As a result, the bulk of the stellar halo originates from just one or two massive dwarf galaxies, such as Gaia-Sausage/Enceladus (GS/E) [Belokurov et al., 2020], while the rest contribute primarily dark matter and kinematic substructure.

The GS/E event, traced by stars with  $-2 < [\text{Fe}/\text{H}] < -1$  and highly radial orbits ( $\beta \gtrsim 0.8$ ), is thought to dominate the inner halo [Belokurov et al., 2018, Helmi et al., 2018]. At lower metallicities ( $[\text{Fe}/\text{H}] \lesssim -2$ ), a broader mix of earlier, minor accretion events likely erases any net rotation [Lancaster et al., 2019, Bird et al., 2021].

Interestingly, stars with low metallicities and modest eccentricities or prograde motion have also been observed [Norris et al., 1985, Chiba and Beers, 2000, Carollo et al., 2019, An and Beers, 2020], even down to  $[\text{Fe}/\text{H}] < -2$  [Sestito et al., 2019, Venn et al., 2020, Cordini et al., 2020, Mardini et al., 2022]. Whether these represent (i) a genuine *in-situ* metal-poor disk or (ii) spun-up debris from early mergers remains debated.

Three disk formation scenarios are proposed:

1. **Early *in-situ* disk.** Stars formed in a gas-rich disk before  $z \sim 4$  and later migrated or were dynamically heated, preserving early chemical signatures.
2. **Massive early mergers.** VMP stars formed in a few massive, gas-rich satellites accreted at high redshift; their debris was deposited into the inner Galaxy as the disk settled [e.g. Sestito et al., 2020].
3. **Late, minor prograde mergers.** Low-mass satellites on aligned orbits were accreted after disk formation, depositing a cool, metal-poor component [Santistevan et al., 2021].

Cosmological simulations generally favour the second scenario, in which early mergers contribute the bulk of the VMP star budget, while a well-defined disk structure forms later, at  $z \lesssim 2$  [Gurvich et al., 2023]. Observationally, Belokurov and Kravtsov [2022] identified *Aurora*, a weakly rotating, kinematically hot population with  $-2 \lesssim [\text{Fe}/\text{H}] \lesssim -1.3$ , arguing against the existence of an extremely early thin disk. Further work shows Aurora to be centrally concentrated [Rix et al., 2022, Arentsen et al., 2020a,b], consistent with heated or spun-up debris rather than a long-lived, coherent disk. Moreover, secular processes such as bar-halo resonances may induce a mild prograde bias [Dillamore et al., 2023], mimicking disk-like kinematics in the halo.

### 1.4 This Work

By reproducing the Extreme Deconvolution Gaussian Mixture Model (XD-GMM) analysis of Zhang et al. [2024], this study re-examines the claim that the Milky Way contains a very-metal-poor ( $[\text{M}/\text{H}] < -2$ ) stellar disk. In successive narrow  $[\text{M}/\text{H}]$  bins, and separately for

the two  $\alpha$  sequences, we model the full velocity distribution ( $v_R, v_\phi, v_z$ ) with an XD-GMM, whose parameters are inferred while explicitly folding each star’s distance and proper-motion covariance into the likelihood. This uncertainty-aware approach prevents measurement noise from biasing the recovered kinematic structure.

Astrophysically, a genuine disk should emerge as a high-weight Gaussian centred around  $v_\phi \simeq 200 \text{ km s}^{-1}$  with small tangential and vertical dispersions and negligible mean radial motion, whereas halo or heated debris appear as broad, nearly isotropic Gaussians with little net rotation. Tracking the weight of the cold, rotating component as a function of metallicity (and  $\alpha$ ) therefore pinpoints the epoch when ordered rotation first arose and tests whether very-metal-poor stars formed in situ or were accreted from satellites.

## 2 Data

### 2.1 Sample construction

The catalogue used in the initial part of this work was the bright red-giant-branch sample of [Andrae et al. \[2023\]](#). This catalogue provides stellar metallicities which were predicted with an Extreme Gradient Boosting model trained on high-resolution APOGEE DR17 spectra and a supplementary set of very metal-poor stars, ensuring reliable performance down to  $[\text{M}/\text{H}] \simeq -3.5$  [[Andrae et al., 2023](#)]. For each of the 17.6 million giants the catalogue contains values of  $[\text{M}/\text{H}]$ ,  $T_{\text{eff}}$ , and  $\log g$  with a random uncertainty of  $\simeq 0.1$  dex in  $[\text{M}/\text{H}]$  at  $G \lesssim 15$ . The catalogue only retains entries flagged as “high-confidence” and lying in  $-3.5 < [\text{M}/\text{H}] < +0.5$ .

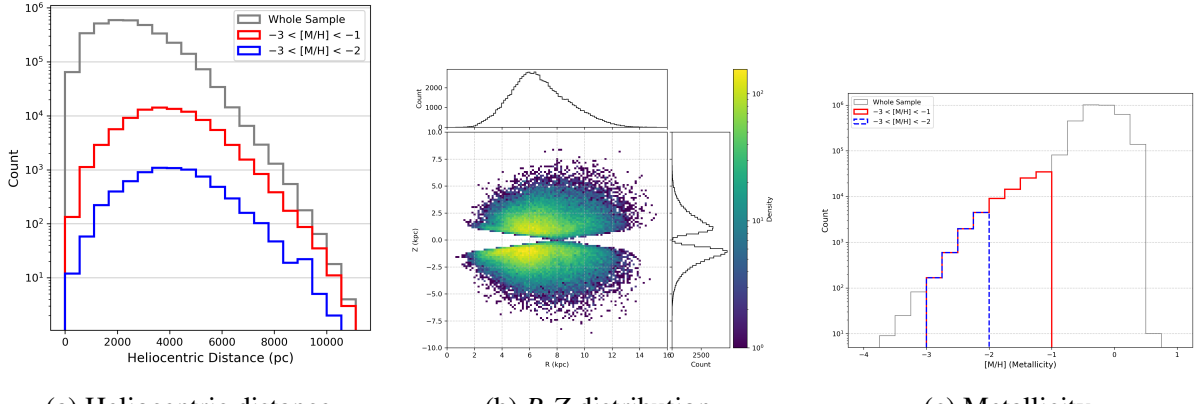
Astrometric positions, proper motions, and radial velocities come from the main *Gaia* DR3 tables [[Gaia Collaboration et al., 2023](#)], while heliocentric distances are adopted from the Bayesian photo-geometric catalogue of [Bailer-Jones et al. \[2021\]](#). Because accurate velocities scale with distance precision, following [Zhang et al. \[2024\]](#), a fractional-parallax-uncertainty cut  $\sigma_\varpi/\varpi < 0.10$  was applied.

XP spectra are susceptible to reddening: heavy extinction dims the sources, lowers the XP signal-to-noise ratio, and biases the machine-learning metallicities. As described [Zhang et al. \[2024\]](#), to minimise such systematics, stars with  $E(B-V)_{\text{SFD}} > 0.5$  or Galactic latitude  $|b| < 10^\circ$  were excluded. Colour-excess values from the SFD map accessed via dustmaps [[Green, 2018](#)] was used for this. These criteria remove regions where dust corrections are large and spatially variable, at the expense of a loss of sky coverage losing a large number of stars at low galactic latitudes.

Field-star kinematics can also be skewed by dense sub-structures. Accordingly, following [Zhang et al. \[2024\]](#), we removed all objects lying within  $1^\circ$  of any known globular cluster or dwarf-galaxy satellite using the list and data of these compiled by [Pace \[2024\]](#). This step removes obvious non-field populations (e.g. cluster members and recent accretion debris) without significantly reducing the statistical power of the sample.

By following the data cuts of [Zhang et al. \[2024\]](#) of distance-quality, reddening, latitude, and sub-structure cuts, our working data set comprised of  $\sim 3.4 \times 10^6$  red-giant stars possessing homogeneous metallicities and six-dimensional phase-space information.

Given we are testing whether a very-metal-poor stellar disk exists, following [Zhang et al. \[2024\]](#), we restrict the sample to stars within  $|Z| < 2.5 \text{ kpc}$  of the galactic mid-plane. This



(a) Heliocentric distance

(b)  $R$ - $Z$  distribution

(c) Metallicity

Figure 1: Properties of the final RGB sample after all quality and footprint cuts. *Left:* heliocentric-distance histogram for the whole sample (grey); the subsets with  $-3 < [M/H] < -1$  and  $-3 < [M/H] < -2$  are shown in solid red and dashed blue, respectively. *Middle:* density map in Galactocentric cylindrical coordinates. The empty band at low  $|Z|$  is a selection artefact of our latitude/extinction cuts, which deliberately remove the thin-disk mid-plane; the concentration around  $R \simeq 5\text{--}8$  kpc reflects the volume accessible to bright RGB stars interior to the Solar circle and coincides with the molecular ring region where the stellar surface density peaks. *Right:* Metallicity distribution of our data sample. Line colours are the same as in the left panel. (A reproduction of Figure 1 from [Zhang et al. \[2024\]](#))

keeps the focus on stars close to the plane, where any disk-like population (whether formed in situ or deposited by mergers) would be found [[Tkachenko et al., 2025](#)].

Upon comparison with [Zhang et al. \[2024\]](#), we note that our sample is approximately the same size - with a difference of less than 0.002% of the sample size in each bin.

## 2.2 Galactocentric Positions and Velocities

Six-dimensional phase-space coordinates were obtained with `astropy.coordinates`. We adopted a Galactocentric frame with  $R_0 = 8.1$  kpc and  $Z_0 = 25$  pc [[McMillan, 2016](#)], and a solar velocity.  $(U_\odot, V_\odot, W_\odot) = (11.1, 245, 7.25)$  km s $^{-1}$  [[Schönrich et al., 2010](#)]. The cylindrical velocity components ( $v_R, v_\phi, v_Z$ ) were extracted using the transformed `SkyCoord` module.

To propagate measurement errors we generated  $N_{MC} = 100$  Monte-Carlo realisations per star, drawing parallax, proper motions, radial velocity, and distance from their reported uncertainties. Each realisation was transformed to the Galactocentric frame, yielding distributions of  $v_R$ ,  $v_\phi$ , and  $v_Z$ ; the  $1\sigma$  widths of those distributions were stored as per-star velocity uncertainties.

Stellar azimuthal velocities evolve increase with metallicity as shown in Figure 2. Halo-like kinematics dominate at  $[M/H] \lesssim -1.5$  with statistics indicative of a pressure-supported component. A spin-up appears over the metallicity range  $[M/H] \simeq -1.3$  to  $-0.9$ , consistent with [Belokurov and Kravtsov \[2022\]](#) and with Figure 2. By  $[M/H] \gtrsim -0.5$  the stellar azimuthal velocities reaches the Local Standard-of-Rest value ( $\approx 220$  km s $^{-1}$ ) and the velocity dispersion dispersion falls, marking the transition to a disk.

As shown in Fig. 3, stars with  $[M/H] \geq -1.0$  have a strong prograde bias in azimuthal velocities, with a peak at  $v_\phi \gtrsim 180$  km s $^{-1}$  and a relatively narrow distribution in  $v_R$ . This is consistent with the thin- and thick-disk ellipses (Fig. 4). Below  $[M/H] \simeq -1.0$  the distribution broadens

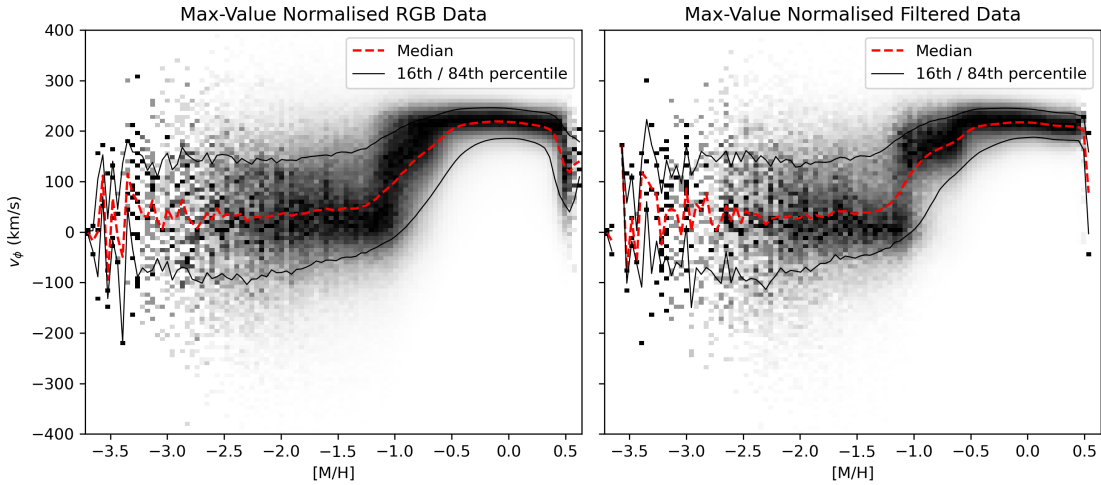


Figure 2: Column-normalised density in the  $v_\phi$ -[M/H] plane. *Left:* the bright-RGB catalogue of Andrae et al. [2023]. *Right:* the same sample after all distance, dust, and quality cuts. Greyscale pixels show the normalised counts in each metallicity bin; the red dashed curve is the median  $v_\phi$ , and the black curves trace the 16<sup>th</sup> and 84<sup>th</sup> percentiles. (A reproduction of Figure 2 from Zhang et al. [2024])

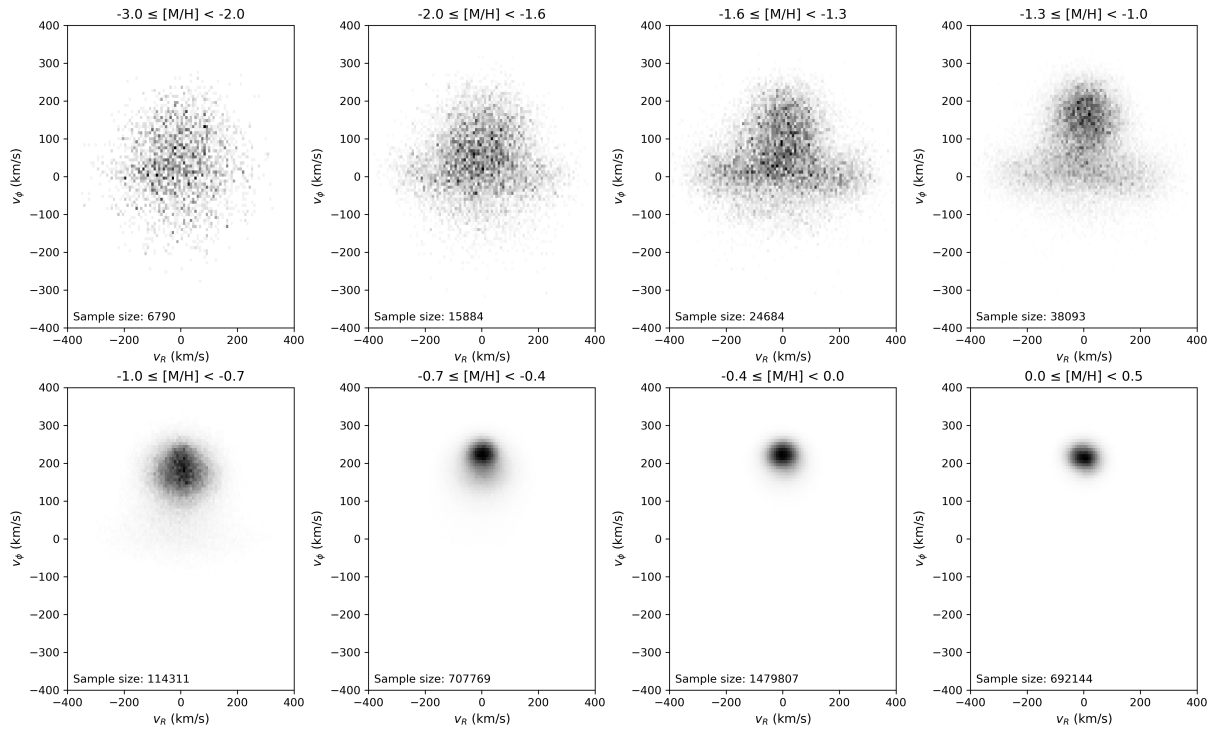


Figure 3: Galactocentric velocity distributions as a function of metallicity. Each panel shows the column-normalised density of stars in the  $v_R$ - $v_\phi$  plane for the metallicity interval printed at the top.(A reproduction of Figure 3 from Zhang et al. [2024])

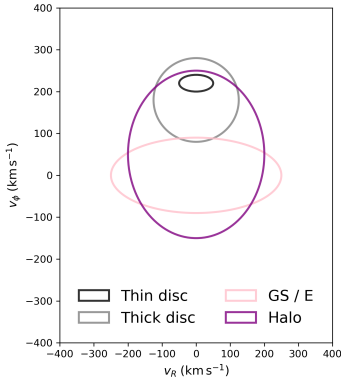


Figure 4: Ellipses mark the approximate extent of the thin disk (black), thick disk (gray), GS/E debris (pink) and the pressure-supported stellar halo (purple). The figure should be used as a visual key for interpreting the data panels in Fig. 3.

and drops toward  $v_\phi \approx 0$ , indicating pressure supported kinematics, characteristic of the stellar halo and the radial GS/E debris. At the lowest metallicities ( $[M/H] \lesssim -1.5$ ) the contours are nearly isotropic with only a mild prograde bias. Hence, any rotation-supported very-metal-poor disk must contribute at most a small fraction of the population. In subsequent analysis we quantitatively assess these observations.

## 3 Methodology

### 3.1 Gaussian Mixture Model

As in [Zhang et al. \[2024\]](#), to quantitatively investigate the kinematic structure of metal-poor stars and assess the presence of a potential very-metal-poor disk, we use a Gaussian Mixture Model (GMM) framework. GMMs are a class of unsupervised machine learning algorithms commonly used in data science for clustering and density estimation. They model a dataset as a weighted sum of multivariate Gaussian distributions, each corresponding to a latent sub-population within the data.

From a probabilistic perspective, the GMM assumes that each observed data point is generated from a hidden (latent) variable indicating membership in one of the Gaussian components. This latent space formulation allows the model to assign probabilistic classifications to data points, providing a soft clustering where each star has a fractional likelihood of belonging to each component. In our case, the data is the three-dimensional velocity vectors  $(v_R, v_\phi, v_Z)$ , and the latent space captures distinct kinematic substructures in this space.

The mixture fitting is carried out with pyGMMis [\[Melchior and Goulding, 2016\]](#) in the full  $(v_R, v_\phi, v_Z)$  phase space. The code implements the *extreme-deconvolution* extension of the Expectation-Maximisation algorithm [\[Bovy et al., 2011\]](#): at every EM iteration each trial Gaussian is *convolved* with the star-specific  $3 \times 3$  velocity-error matrix supplied by Gaia. In doing so, the procedure fit directly for the *intrinsic* (noise-free) velocity distribution, accounting for measurement uncertainties and preventing them from creating or erasing kinematic structure—thereby placing all subsequent disk/halo classifications on a statistically robust footing.

## 3.2 Number of Gaussian Components

We run the XD-GMM in successive 0.3-dex slices across the regime  $[M/H] < -1$ , the only metallicity range where an undiscovered very-metal-poor disk could plausibly reside. Treating each slice independently removes the steep disk gradient in  $[M/H]$  and allows the algorithm to search for rotation-supported structure at a fixed chemical epoch. Within every slice the optimal number of Gaussians,  $k$ , is chosen by the Bayesian Information Criterion (BIC [Schwarz 1978](#): selecting too few components would blur distinct populations together and mask a genuine disk, whereas too many would shatter the halo into noise-driven shards and produce an over-fit, physically meaningless solution.

The BIC is defined as

$$\text{BIC} = k \ln(n) - 2 \ln \mathcal{L}, \quad (1)$$

where  $k = (1 + 3 + 6) \times N - 1$  is the total number of free parameters in a model with  $N$  Gaussian components (accounting for the weights, means, and covariances),  $n$  is the number of stars in the sample, and  $\mathcal{L}$  is the maximum likelihood of the fit. The BIC penalizes model complexity, such that adding extra components without a significant gain in likelihood will result in a higher BIC value.

The Expectation-Maximisation algorithm can become trapped in local minima because the likelihood surface of a Gaussian mixture is highly non-convex: overlapping components, label permutations and sparsely sampled regions generate many secondary peaks, and EM (being a purely uphill optimiser) has no built-in mechanism for escaping the first peak it reaches. To minimise this risk we ran 50 independent initialisations for every candidate component number  $N$ , each time seeding the means with  $k$ -means initialisation on the  $(v_R, v_\phi, v_z)$  data. The  $k$ -means start-up partitions the velocity space into compact, nearly spherical groups that match the Gaussian assumption, giving EM a stable launch point and accelerating convergence. For every run we logged the BIC and adopted the mixture with the lowest BIC overall. This multi-start,  $k$ -means-seeded strategy reduces the chance of local-minimum entrapment and makes it highly likely that the selected model represents the global maximum-likelihood, and therefore statistically preferred, description of the data.

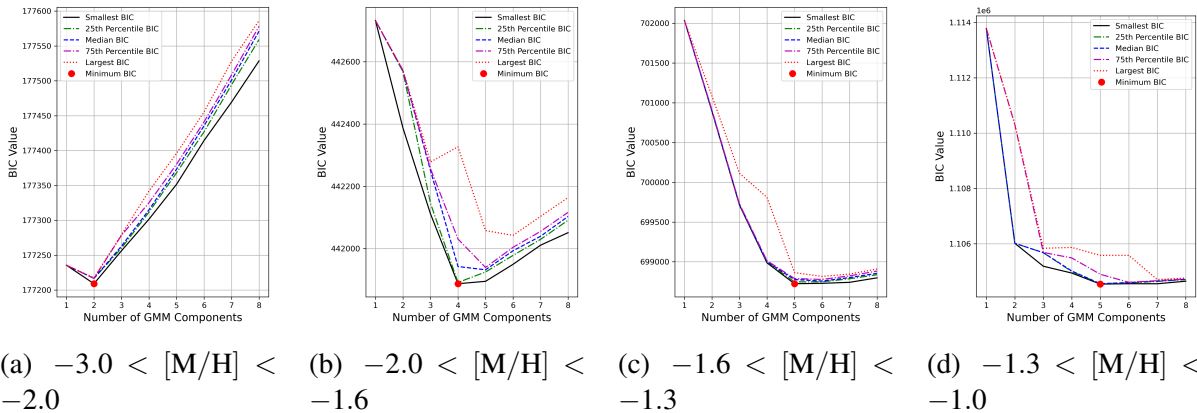


Figure 5: BIC distributions as a function of the number of GMM components in each metallicity bin. The optimum number of components is indicated by the minimum BIC value (highlighted in red). (A reproduction of Figure 4 from [Zhang et al. \[2024\]](#))

In Figure 5, we show the distribution of BIC values across four metallicity bins as a function of  $N$ . The resulting preferred number of components are 2, 4, 5, and 5 for the VMP, IMP, MP1, and MP2 bins. This is in agreement with the findings of Zhang et al. [2024]. Our analysis selects the lowest BIC for each bin, removing the need for a subjective choice of the number of components when BIC values are very similar. Zhang et al. [2024], when observing the BIC values for the MP1 bin chooses to use 5 components instead of 6 despite the BIC score for the 6-component model being lower than the 5-component model.

## 4 Results

### 4.1 Gaussian Mixture Model Fit

Using the number of components selected by the BIC criteria, we fit the GMM to the data in each metallicity bin as shown in Figure 6. We increased the number of initialisations to 100 for the final fitting to ensure convergence to a stable solution.

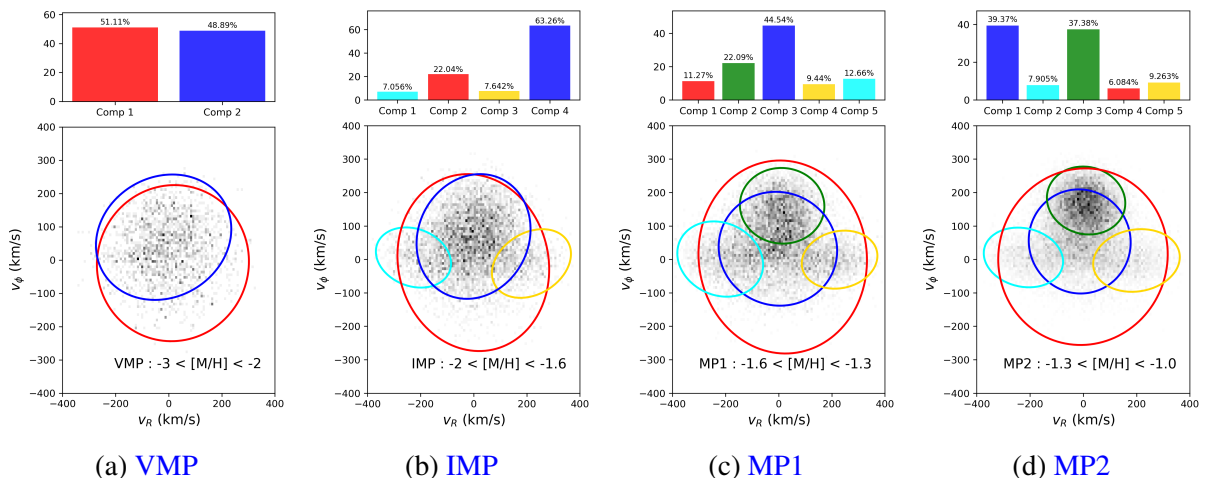


Figure 6: Gaussian Mixture Model decompositions of the stellar velocity distribution in the  $v_R$ - $v_\phi$  plane for each metallicity bin. The lower panels show the 2D  $v_R$ - $v_\phi$  distributions with GMM components overplotted as  $1\sigma$  ellipses, and the upper panels display each component's fractional contribution. (Reproduced from Zhang et al. 2024 Figure 5.) Links to the fully interactive 3-D plots for each bin are provided as hyperlinks in the subcaptions.

As shown in Figure 6, the GMM is able to capture kinematic substructures in the velocity space of metal-poor stars. As metallicity increases, a gaussian component with a clear prograde rotation signal emerges (in green), indicative of a disk-like structure. The statistics of the GMM fit are summarised in Table 1, which lists the weights, means, and dispersions of each component in the four metallicity bins.

At  $[M/H] < -1.6$  (the VMP and IMP regimes), a disk component is not observed. Instead, the kinematic structure is dominated by a prograde halo and a stationary halo. In the VMP bin, the sample is almost evenly split between these two components, with the stationary halo contributing 51.1% and the prograde halo 48.9%. Both show broad velocity dispersions, with only modest rotational support ( $\overline{v_\phi} \sim 69 \text{ km s}^{-1}$  for the prograde halo) and no evidence for a kinematically cold disk-like structure.

<b>Components</b>	<b>Weights (%)</b>	<b>v<sub>R</sub></b>	<b>σ<sub>R</sub></b>	<b>v<sub>ϕ</sub></b>	<b>σ<sub>ϕ</sub></b>	<b>v<sub>Z</sub></b>	<b>σ<sub>Z</sub></b>
<b>VMP:</b> $-3.0 < [\text{M}/\text{H}] < -2.0$ (4768 stars)							
Stationary halo	51.1	15.86	143.17	-9.13	117.36	-0.08	122.64
Prograde halo	48.9	-19.14	127.43	68.86	94.28	-0.90	82.89
<b>IMP:</b> $-2.0 < [\text{M}/\text{H}] < -1.6$ (12052 stars)							
Stationary halo	22.0	-1.45	142.88	-9.59	132.32	-0.91	124.92
Prograde halo	63.3	-0.58	107.32	68.52	93.27	-1.16	72.56
GS/E(1)	7.1	-226.92	70.78	5.60	44.98	8.43	88.40
GS/E(2)	7.6	217.52	74.41	-12.35	51.35	-4.22	89.78
<b>MP1:</b> $-1.6 < [\text{M}/\text{H}] < -1.3$ (19142 stars)							
Stationary halo	11.3	15.09	158.68	7.11	144.33	-2.55	132.08
Prograde halo	44.5	-3.02	111.54	31.79	85.15	-0.54	70.36
GS/E(1)	12.7	-220.40	80.76	1.01	56.29	0.47	91.00
GS/E(2)	9.4	229.32	71.22	-0.82	43.42	1.42	92.69
Thick disk	22.1	12.93	79.56	160.32	56.58	-2.31	68.83
<b>MP2:</b> $-1.3 < [\text{M}/\text{H}] < -1.0$ (30892 stars)							
Stationary halo	6.1	-1.17	159.06	8.07	132.05	-3.37	120.46
Prograde halo	39.4	-13.47	95.65	53.64	77.86	-3.04	71.00
GS/E(1)	7.9	-224.68	74.44	5.73	44.63	2.41	87.27
GS/E(2)	9.3	199.71	81.28	-3.30	46.84	-2.07	88.99
Thick disk	37.4	10.56	73.55	176.07	50.79	0.85	62.03

Table 1: Parameters of the Gaussian mixture model fittings in different metallicity bins. The unit for all velocity columns is  $\text{km s}^{-1}$ .

In the IMP bin, the picture remains similar, although the prograde halo dominates more strongly (63.3%) and additional substructure becomes apparent. Two minor components, interpreted as fragments of the GS/E merger debris, are also identified, each contributing  $\sim 7\%$  of the population and exhibiting highly radial orbits ( $|v_R| > 200 \text{ km s}^{-1}$ ). These GS/E components are characterised by strong anisotropy and contribute to the broadening of the halo distribution, but again show no signature of disk-like kinematics. The absence of a cold, rotating disk in these bins suggests that if a very-metal-poor disk exists, it must be a minor contributor to the local stellar population.

Our GMM decomposition recovers the same substructures identified by [Zhang et al. \[2024\]](#) across all metallicity bins. We find similar velocity dispersions and centroid trends for the stationary halo, prograde halo, and GS/E components. Notably, our model assigns a more comparable weight to the prograde halo component in the VMP bin, in contrast to the dominant stationary halo reported by [Zhang et al. \[2024\]](#). We also observe some variation in the centroid  $v_\phi$  values of GS/E substructures, although their bimodal spatial structure is preserved.

## 4.2 Rotational Support and the Onset of Disk Formation

To assess the degree of rotational support in each component, we compute the ratio  $V_{\text{rot}}/\sigma_\phi$ , where  $V_{\text{rot}}$  is the mean azimuthal velocity and  $\sigma_\phi$  its dispersion. This ratio serves as a conventional diagnostic of disk-like kinematics, with values  $\gtrsim 3$  indicating rotation-supported populations. As shown in Figure 7, all components in the VMP and IMP bins fall below this threshold, confirming that the GMM identifies only dynamically hot, dispersion-supported structures in

these regimes.

At higher metallicities, a dynamically colder disk population emerges. In the MP1 bin, the thick disk component (green) rotates at  $v_\phi \sim 160 \text{ km s}^{-1}$  with  $\sigma_\phi \sim 57 \text{ km s}^{-1}$ , yielding  $V_{\text{rot}}/\sigma_\phi \approx 2.8$ . While just below the canonical boundary, this component's low vertical dispersion and substantial weight (22.1%) mark it as a distinct disk-like structure. By the MP2 bin, the disk becomes the dominant component (37.4%), with  $V_{\text{rot}}/\sigma_\phi \approx 3.5$ , indicating clear rotational support and a well-established thick disk. These trends suggest a transition in the stellar kinematics around  $[\text{M}/\text{H}] \sim -1.5$ .

Meanwhile, the GS/E components (identifiable in the IMP, MP1, and MP2 bins) remain dynamically distinct, with high  $|v_R|$ , relatively small  $v_\phi$ , and negligible rotational support, reinforcing their origin as debris from a major radial merger [Helmi et al., 2018]. Notably, given the estimated time of the GS/E accretion event (of order 8-11 Gyr ago [Gallart et al., 2019, Belokurov et al., 2020, Di Matteo et al., 2019]), its stellar debris is expected to be phase-mixed. This implies that the positive and negative  $v_R$  components should contribute approximately equally. This symmetry is observed in the IMP and two MP bins.

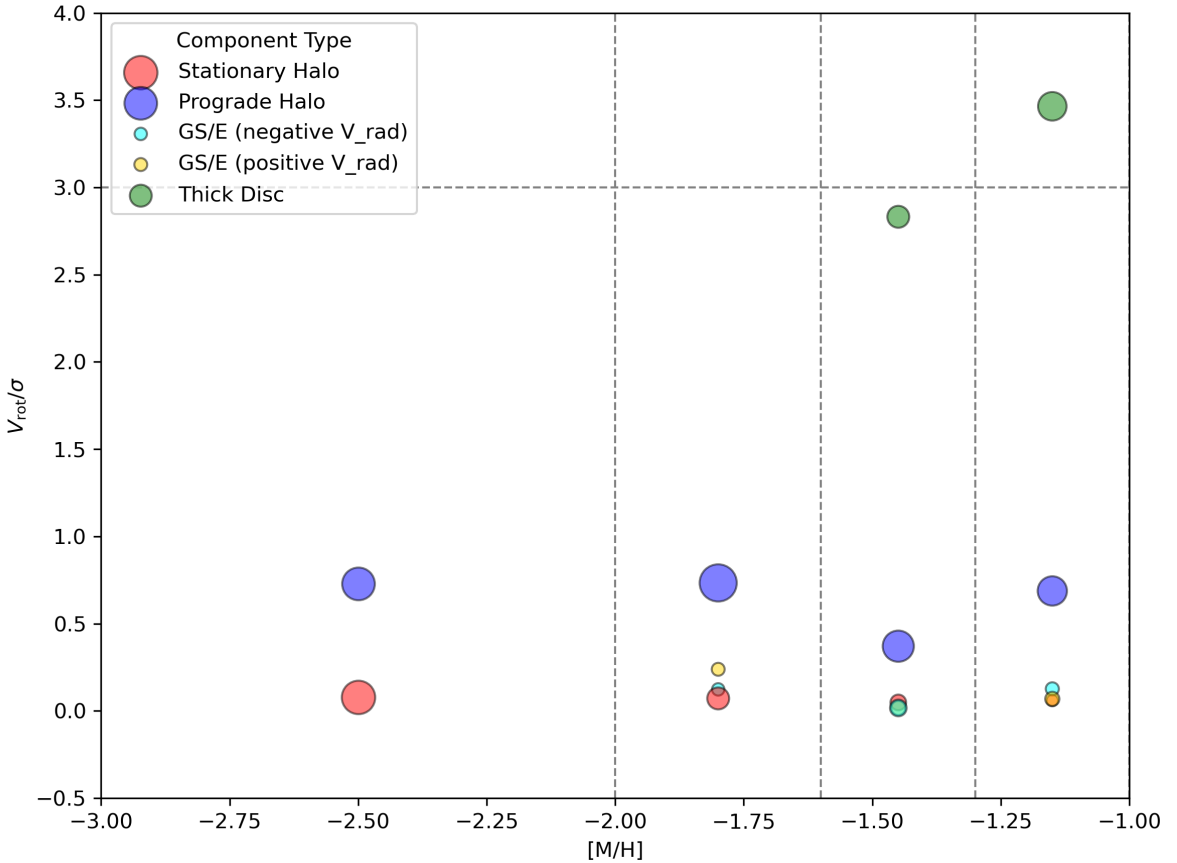


Figure 7: Ratio of mean rotational velocity to azimuthal velocity dispersion,  $V_{\text{rot}}/\sigma_\phi$ , for individual GMM components in each metallicity bin. Larger circles correspond to more dominant components. Colours match the GMM components in Figure 6.(A reproduction of Figure 6 from Zhang et al. [2024])

### 4.3 Residual Analysis for Hidden Disk Populations

One of the limitations of GMMs is that they can fail to detect substructures that contribute only weakly to the overall distribution. To investigate this, we performed a residual analysis to test whether a disk-like population, too weak to be picked up by the GMM, might be present in the VMP and IMP metallicity regimes.

Following [Zhang et al. \[2024\]](#), we generated a synthetic dataset by drawing the same number of mock stars as observed stars from the best-fit GMM in each bin. Since our GMM uses the Extreme Deconvolution algorithm, which accounts for observational uncertainties during fitting, the raw samples from the model are noise-free. However, comparing these directly to real data would be inappropriate due to the absence of measurement error. To resolve this, we assign each mock star the velocity uncertainties of its nearest neighbour in the observed data (in  $(v_R, v_\phi, v_Z)$  space), and then add Gaussian noise according to these uncertainties.

We then bin both the observed and mock data in the  $(v_R, v_\phi)$  plane and compute the normalized residual map, defined as

$$H_{\text{residual}} = \frac{H_{\text{obs}} - H_{\text{mock}}}{H_{\text{obs}} + H_{\text{mock}} + \epsilon},$$

where  $H_{\text{obs}}$  and  $H_{\text{mock}}$  are the 2D histograms and  $\epsilon = 10^{-5}$  is added to avoid division by zero. The residual maps are shown in the top row of Figure 8 for the VMP and IMP bins. The grey dashed ellipses highlight a  $2\sigma$  region of a hypothetical thick disk with mean velocity  $(v_R, v_\phi) = (0, 180) \text{ km s}^{-1}$  and dispersions  $(\sigma_R, \sigma_\phi) = (70, 50) \text{ km s}^{-1}$ , consistent with the thick disk component seen in the MP2 metallicity bin.

To quantify the possible presence of a hidden disk, we count the excess number of observed stars inside this thick disk ellipse relative to the GMM-generated sample. We repeat this calculation for 1000 Monte Carlo realisations to estimate the residual and its uncertainty. The results are shown as horizontal dashed lines in the bottom row of Figure 8, representing a disk-like residual of  $38.3 \pm 27.1$  stars in the VMP bin and  $78.1 \pm 45.1$  stars in the IMP bin.

To interpret these residuals, we repeat the same procedure but now inject a mock disk population—generated from the same thick disk Gaussian—into the GMM baseline. By varying the injected disk fraction from 0% to 5% of the sample and recalculating the residual each time, we construct a relationship between disk fraction and expected residual. This is shown as the solid black line in the bottom panels of Figure 8, with the red shaded region indicating the  $1\sigma$  uncertainty across Monte Carlo trials.

The intersection of the solid and dashed lines could imply a hidden disk fraction of up to  $\sim 1\%$  in the VMP bin and IMP bin. Interestingly, the overlap of these lines in the IMP bin occurs at a lower percentage. These estimates are indicative only: measurement uncertainties, GMM modelling choices, and Gaia-selection cuts mean that the true disk contribution in the parent VMP/IMP populations may differ [[Zhang et al., 2024](#)].

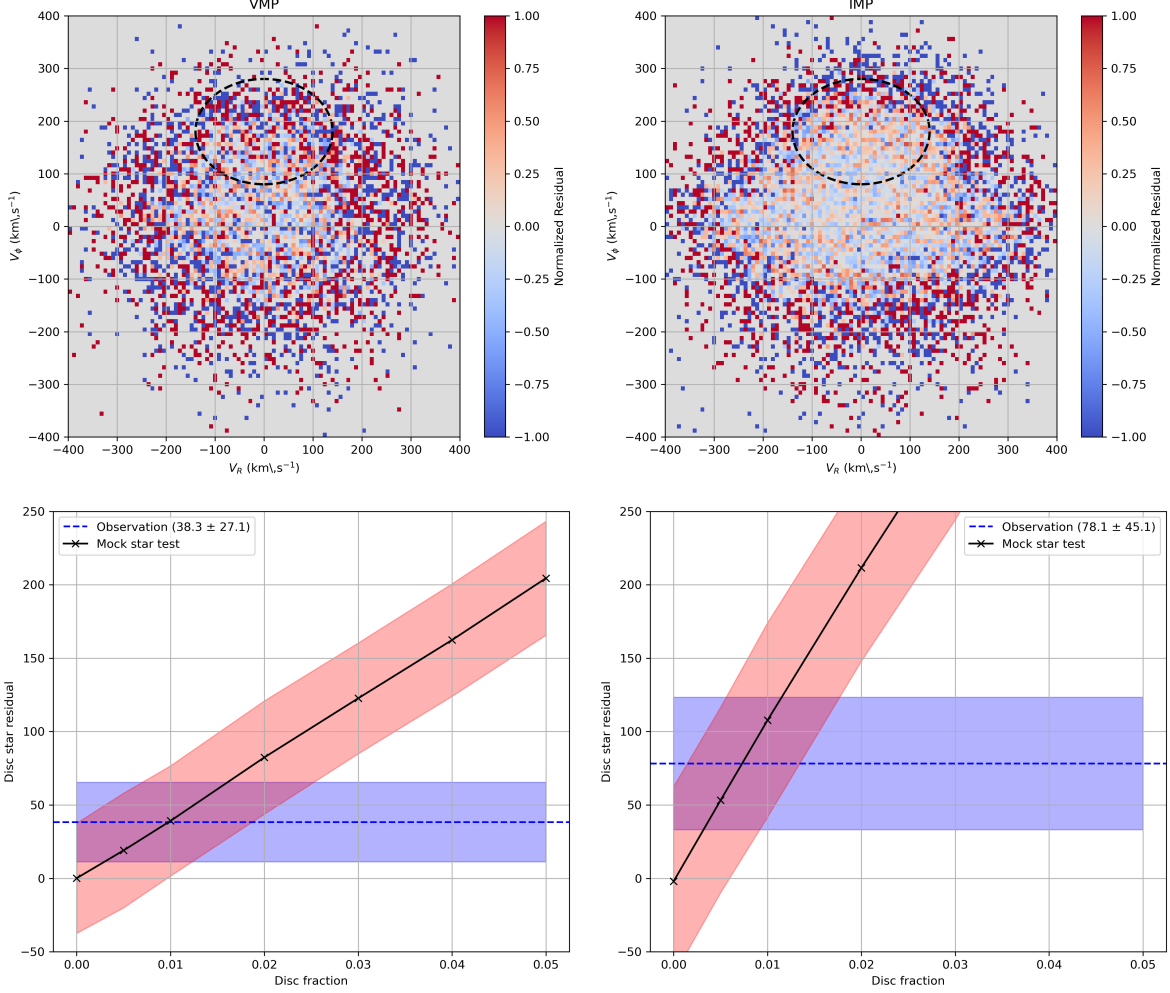


Figure 8: Top: Normalised residual maps between observed and GMM-predicted velocity distributions in  $(v_R, v_\phi)$  for the VMP (left) and IMP (right) metallicity bins. Grey ellipses show the  $2\sigma$  contour of the fiducial thick disk model. Bottom: Disk residuals as a function of injected disk fraction. The dashed line and blue band indicate the observed residual and its uncertainty. The solid black line and red region show mock test results and their uncertainties. (A reproduction of Figure 7 from [Zhang et al. \[2024\]](#))

## 5 Extension Analysis

We extend the work of [Zhang et al. \[2024\]](#) by adding the  $\alpha$ -element abundance,  $[\alpha/\text{Fe}]$ , as a fourth dimension in our XD-GMM fits. Following [Viswanathan et al. \[2024\]](#), each metallicity bin is split into “high- $\alpha$ ” and “low- $\alpha$ ” subsets (using XP abundances from [Li et al. 2023](#)), and the GMM is refit independently for each subset. This chemo-kinematic dissection allows us to test whether the kinematic substructures in the very-metal-poor regime vary with  $\alpha$ -element enrichment, potentially distinguishing in situ from accreted populations.

### 5.1 Alpha-Element Abundance

The ratio  $[\alpha/\text{Fe}]$  traces the relative contributions of two supernova types: core-collapse (Type II) and thermonuclear (Type Ia). Type II supernovae result from the deaths of massive stars

( $\gtrsim 8 M_{\odot}$ ) and explode on short timescales ( $\sim 10$ – $30$  Myr) after star formation. They produce large amounts of  $\alpha$ -elements (O, Ne, Mg, Si, S, Ca, Ti), which are rapidly injected into the interstellar medium. In contrast, Type Ia supernovae arise from white dwarfs in binary systems, requiring hundreds of millions to billions of years to explode ( $\gtrsim 0.1$ – $1$  Gyr). These events primarily enrich the interstellar medium with iron and iron-peak elements (e.g. Fe, Ni, Co).

Because the two channels operate on different timescales, the  $[\alpha/\text{Fe}]$  ratio encodes a population’s formation history:

- **High- $[\alpha/\text{Fe}]$ :** Rapid, intense star formation enriches the gas with  $\alpha$ -elements before Type Ia supernovae contribute significant iron, leading to elevated  $[\alpha/\text{Fe}]$ . These stars typically belong to the in-situ thick disk, stellar halo, and ancient accreted debris. At fixed  $[\text{M}/\text{H}]$ , accreted populations (e.g. dwarf galaxies) generally show lower  $[\alpha/\text{Fe}]$  than in-situ stars [Helmi et al., 2018], reflecting slower chemical evolution.
- **Low- $[\alpha/\text{Fe}]$ :** A more extended star-formation history allows iron from Type Ia supernovae to accumulate, diluting the  $\alpha$  enrichment. This regime includes the thin disk, metal-rich bulge, and remnants of dwarf satellites.

Hence, in the  $[\alpha/\text{Fe}]$ – $[\text{M}/\text{H}]$  plane, populations that overlap in metallicity but formed on different timescales separate cleanly in  $\alpha$  enrichment. By fitting separate XD-GMMs to the high- and low- $\alpha$  sequences within each metallicity bin, we can isolate how disk-like rotation and halo substructures depend on chemical evolution history.

## 5.2 Data

We obtain the  $\alpha$ -to-metal abundance ratios from the XP-based catalogue of Li et al. [2023]. Following Viswanathan et al. [2024], we cross-match the XP-based  $\alpha$  catalogue of Li et al. [2023] with the metallicity-selected red-giant branch sample. This base sample already incorporates the red-giant selection and photometric quality cuts from Andrae et al. [2023], including limits on surface gravity, colour–magnitude position, and XP calibration reliability.

To further ensure robust  $\alpha$  abundances and kinematics, we apply same cuts as in Section 2.1, however we relax the fractional parallax uncertainty cut requiring only  $fpu < 0.2$  to retain sufficient stars in the metal-poor regime. We obtain approximately 3.4 million stars in our final sample with alpha-element abundances.

Figure 9 shows the logarithmic density of our RGB sample in the  $[\alpha/\text{M}]$ – $[\text{M}/\text{H}]$  plane. Following Chandra et al. [2024], but with a deliberately tighter boundary as defined in Viswanathan et al. [2024]:

$$\begin{aligned} \text{high-}\alpha : & \begin{cases} [\text{M}/\text{H}] < -0.60 & [\alpha/\text{M}] > 0.28 \\ -0.60 \leq [\text{M}/\text{H}] \leq 0.125 & [\alpha/\text{M}] > -0.25[\text{M}/\text{H}] + 0.13 \\ [\text{M}/\text{H}] > 0.125 & [\alpha/\text{M}] > 0.10 \end{cases} \\ \text{low-}\alpha : & \begin{cases} [\text{M}/\text{H}] < -0.80 & [\alpha/\text{M}] < 0.21 \\ -0.80 \leq [\text{M}/\text{H}] \leq 0.07 & [\alpha/\text{M}] < -0.21[\text{M}/\text{H}] + 0.04 \end{cases} \end{aligned}$$

Viswanathan et al. [2024] raise the high- $\alpha$  threshold so that the chemistry of the GS/E debris [Belokurov et al., 2018, Helmi et al., 2018] does not leak into the in-situ sequence; the exclusion

band between the branches is widened to maximise purity in both sub-samples [Viswanathan et al., 2024].

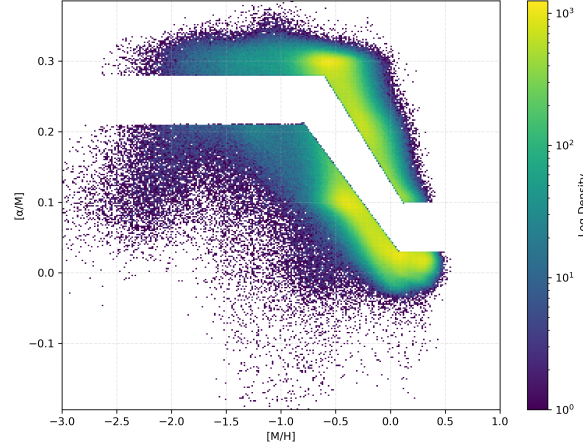
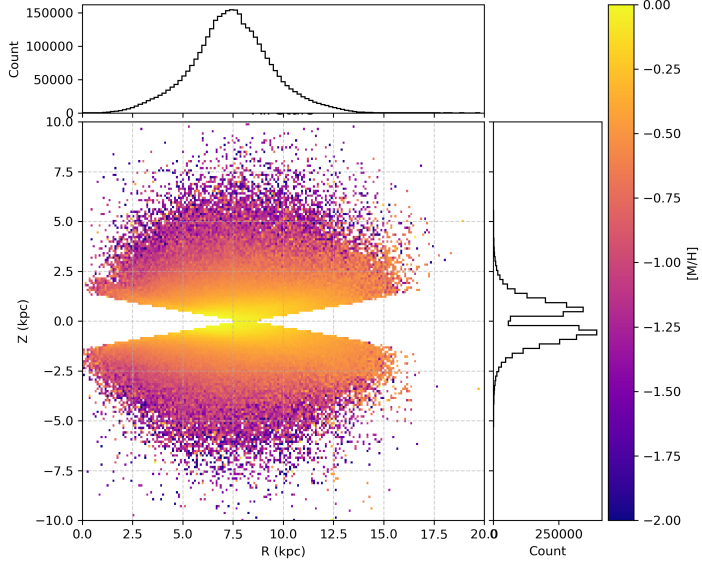
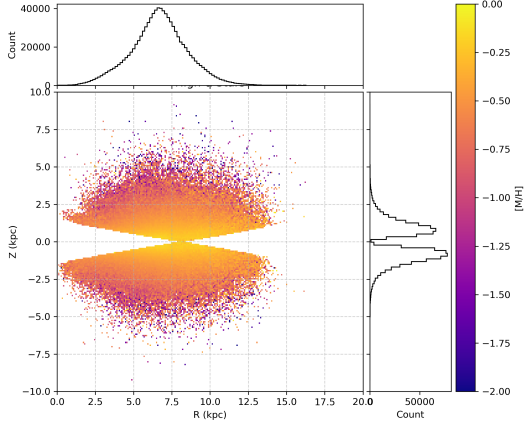


Figure 9: Density of stars in the  $[\alpha/M]$ – $[M/H]$  plane. The high- $\alpha$  and low- $\alpha$  sequences are separated by the piecewise linear boundary described in the text. The transition zone between the two sequences is clearly removed from this plot and discarded from subsequent analysis. (A reproduction of Figure 1 in Viswanathan et al. [2024])

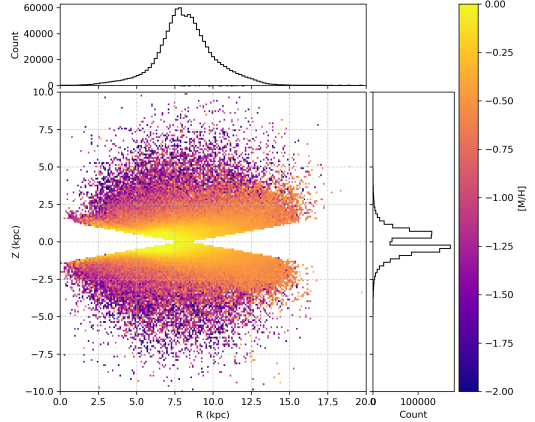
Figure 10 shows the distribution of our sample in cylindrical Galactocentric radius  $R$  versus height above the midplane  $z$ , colour-coded by the mean metallicity in each pixel. The top panel presents this distribution for the full RGB sample, while the bottom panels split the data into high- $\alpha$  (left) and low- $\alpha$  (right) subsamples.



(a) All RGB stars



(b) High- $\alpha$  subsample



(c) Low- $\alpha$  subsample

Figure 10: Mean  $[M/H]$  colour-coded in the Galactocentric  $R-z$  plane. *Top:* the complete  $G < 16$  RGB sample. *Bottom left:* high- $\alpha$  stars; *bottom right:* low- $\alpha$  stars. The high- $\alpha$  population is more centrally concentrated and shows a shallower vertical metallicity gradient. (A reproduction of Figure 2 in [Viswanathan et al. \[2024\]](#))

A steep negative metallicity gradient with increasing  $z$  is evident in the low- $\alpha$  sample and also visible in the full sample, likely due to the dominance of low- $\alpha$  stars in the overall dataset. In contrast, the high- $\alpha$  population exhibits a shallower vertical metallicity gradient and a thicker disk structure. We also observe a metallicity gradient towards larger  $R$  in the low- $\alpha$  disk, indicative of radial migration and consistent with flaring commonly seen in the Galactic thin disk [e.g. [Haywood et al., 2013](#), [Ratcliffe et al., 2023](#)].

To trace how rotational support evolves with metallicity and  $\alpha$ -element enrichment, following [Viswanathan et al. \[2024\]](#) we examine the distribution of azimuthal velocity ( $v_\phi$ ) as a function of  $[M/H]$ :

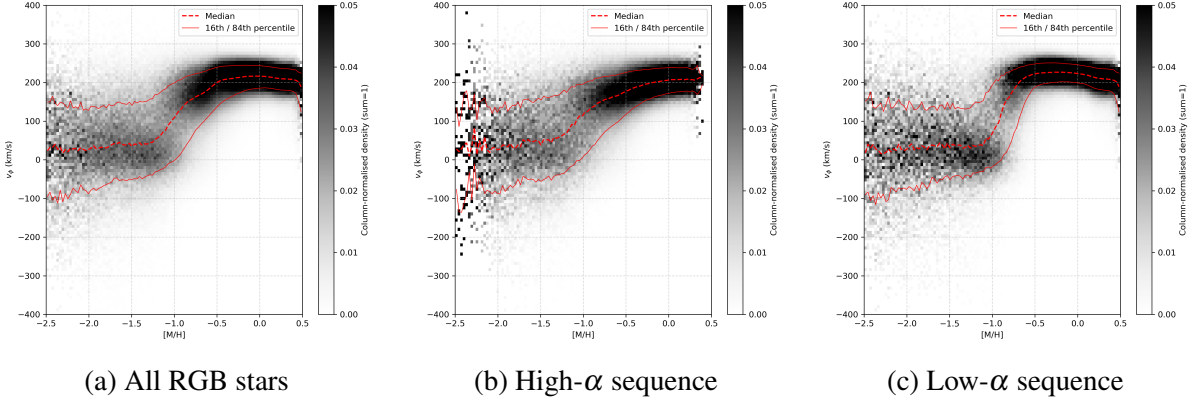


Figure 11: Azimuthal velocity versus metallicity. Left: full RGB sample. Centre: high- $\alpha$  stars. Right: low- $\alpha$  stars. Contours show running medians (red) and the 16th/84th percentiles (black). (Adapted from Fig. 3 of [Viswanathan et al. 2024](#).)

The high- $\alpha$  giants exhibit a gradual spin-up with increasing metallicity. At low metallicities ( $[M/H] \lesssim -2$ ), the population shows mild net prograde rotation with large dispersion, consistent with a dynamically hot stellar halo. From  $[M/H] \gtrsim -1.3$ , there is a steady increase in rotation velocity and a corresponding decrease in dispersion, indicative of a transition toward the thick disk. By  $[M/H] \gtrsim -0.5$ , most stars occupy a kinematic regime characterised by elevated  $v_\phi$  and moderate dispersion, consistent with a dynamically hot but rotationally supported thick disk. This continuous trend supports a scenario in which the Galaxy’s in-situ population gradually acquired angular momentum as star formation progressed.

In the low- $\alpha$  panel, stars with  $[M/H] \lesssim -1.2$  exhibit kinematics similar to those in the high- $\alpha$  sequence, showing mild prograde rotation and high velocity dispersion. However, above  $[M/H] \gtrsim -1.2$ , the low- $\alpha$  sequence undergoes a sharper transition to a population with high net prograde rotation and lower velocity dispersion. By  $[M/H] \gtrsim -0.5$ , the low- $\alpha$  population exhibits kinematics consistent with the thin disk: a strongly rotating, dynamically colder component with lower dispersion than the high- $\alpha$  sequence.

### 5.3 Gaussian Mixture Model Fit

We follow the same Gaussian mixture model fitting procedure as in Section 4.1, but now separately for the high- and low- $\alpha$  sequences.

$\alpha$ -Sequence	VMP ( $[M/H] < -2.0$ )	IMP ( $-2.0 < [M/H] < -1.3$ )	MP1 ( $-1.3 < [M/H] < -1.0$ )	MP2 ( $-1.0 < [M/H] < -0.7$ )
High- $\alpha$	1	4	5	3
Low- $\alpha$	1	2	3	5

Table 2: Number of Gaussian Mixture components selected by the BIC for each metallicity bin, split by  $\alpha$ -sequence.

Following the methodology described in Section 3.2, Table 2 summarises the number of components selected by the Bayesian Information Criterion for each metallicity bin. Detailed BIC scores for each metallicity bin are shown in Figure 12.

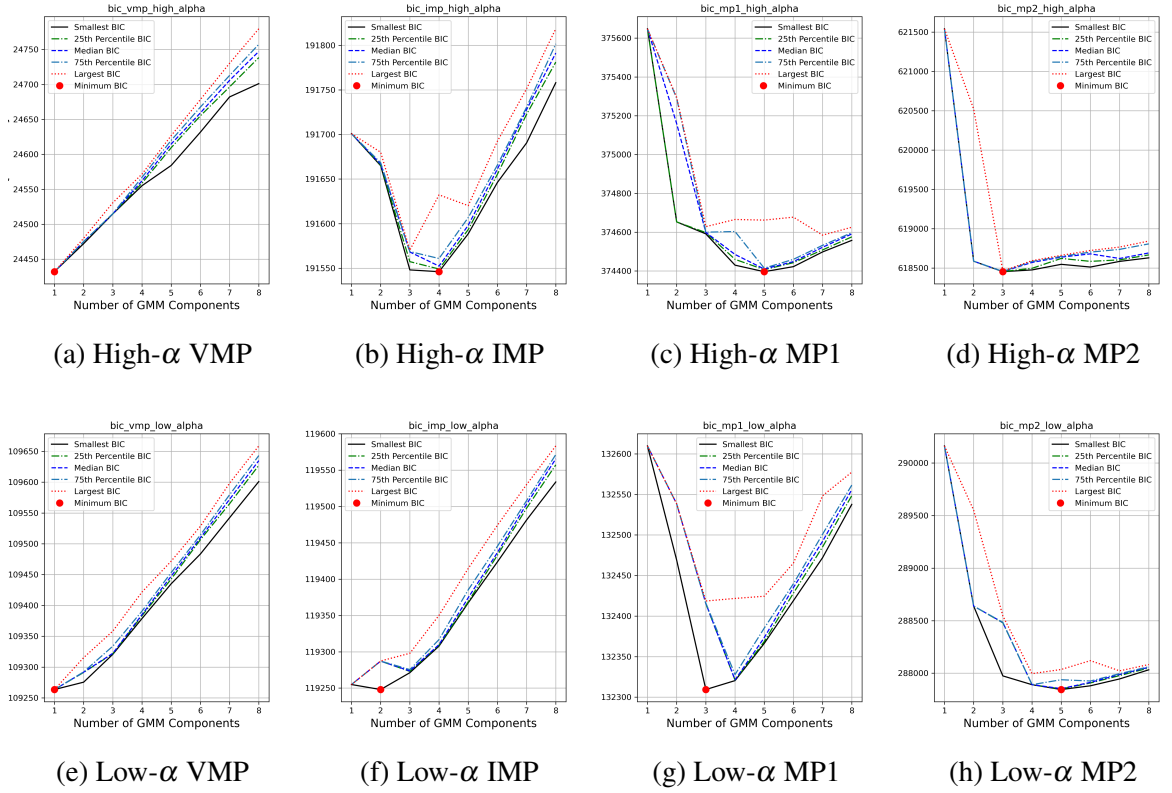


Figure 12: BIC scores for different metallicity bins, grouped by high- and low- $\alpha$  populations.

## 5.4 High alpha Gaussian Mixture Model Fit

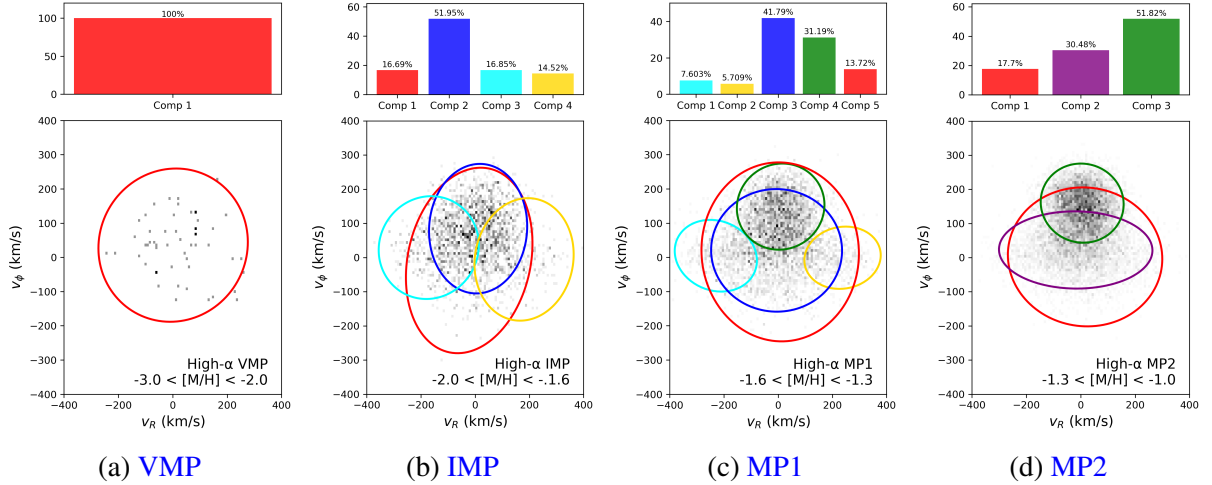


Figure 13: XD–GMM decomposition of high- $\alpha$  giants in four metallicity bins. Grey ellipses mark the  $1\sigma$  contours of each Gaussian component; click the subcaptions to open the interactive 3D plots.

Components	Weights (%)	$v_R$	$\sigma_R$	$v_\phi$	$\sigma_\phi$	$v_Z$	$\sigma_Z$
<b>VMP:</b> $-3.0 < [M/H] < -2.0$ (657 stars)							
Stationary halo	100.0	1.40	137.36	35.59	111.99	7.60	102.48
<b>IMP:</b> $-2.0 < [M/H] < -1.6$ (5219 stars)							
Stationary halo	16.7	-22.06	116.74	-8.55	135.74	-2.64	125.40
Prograde halo	51.9	10.84	90.56	84.51	94.79	-0.76	69.42
GS/E (1)	16.8	-171.35	92.33	29.12	75.23	0.50	87.09
GS/E (2)	14.5	180.48	91.48	-5.47	89.66	-2.87	94.37
<b>MP1:</b> $-1.6 < [M/H] < -1.3$ (10265 stars)							
Stationary halo	13.7	7.44	145.24	15.90	130.80	-8.97	127.11
Prograde halo	41.8	-5.85	120.77	20.31	89.59	-1.29	72.85
GS/E (1)	7.6	-230.09	75.81	4.65	52.41	8.69	94.68
GS/E (2)	5.7	237.61	70.43	-1.23	45.51	-3.73	92.81
Thick disk	31.2	9.18	80.79	148.23	62.97	2.99	68.92
<b>MP2:</b> $-1.3 < [M/H] < -1.0$ (17314 stars)							
Stationary halo	17.7	15.91	141.96	2.13	101.75	-1.68	98.90
GS/E	30.5	-18.50	141.08	22.42	56.55	-2.40	77.98
Thick Disk	51.8	5.22	76.27	159.54	57.94	-0.83	67.18

Table 3: GMM component weights and kinematics for the high- $\alpha$  sequence. Velocities are in  $\text{km s}^{-1}$ . Weights indicate the fraction of stars per metallicity bin.

## 5.5 Low alpha Gaussian Mixture Model Fit

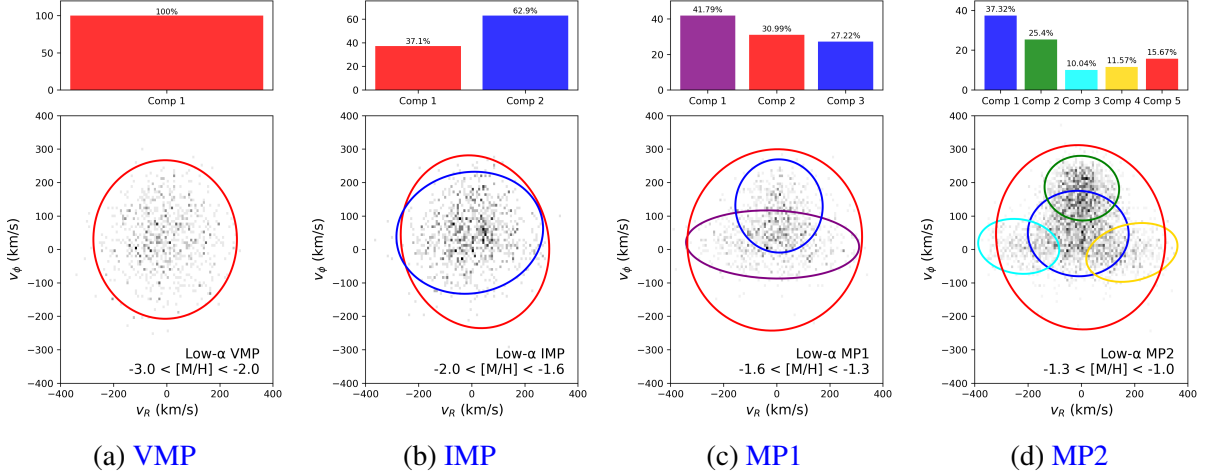


Figure 14: XD-GMM decomposition of low- $\alpha$  giants in four metallicity bins. Grey ellipses show the  $1\sigma$  contours of every Gaussian component; click the subcaptions to open the interactive 3D plots.

Components	Weights (%)	$v_R$	$\sigma_R$	$v_\phi$	$\sigma_\phi$	$v_Z$	$\sigma_Z$
<b>VMP:</b> $-3.0 < [\text{M}/\text{H}] < -2.0$ (2929 stars)							
Stationary halo	100.0	-5.82	135.18	29.55	118.56	1.34	107.10
<b>IMP:</b> $-2.0 < [\text{M}/\text{H}] < -1.6$ (3228 stars)							
Stationary halo	37.1	12.33	139.85	22.87	129.23	-4.43	120.51
Prograde halo	62.9	-7.34	138.11	49.68	91.25	4.08	75.99
<b>MP1:</b> $-1.6 < [\text{M}/\text{H}] < -1.3$ (3603 stars)							
Stationary halo	31.0	-7.58	164.57	28.31	135.62	-4.92	121.66
GS/E	41.8	-15.50	162.97	14.71	50.94	-1.93	73.60
Thick Disk/prograde halo	27.2	8.72	82.25	129.87	69.71	3.13	60.68
<b>MP2:</b> $-1.3 < [\text{M}/\text{H}] < -1.0$ (7945 stars)							
Stationary halo	15.7	-2.30	158.84	36.24	137.81	2.81	131.10
Prograde halo	37.3	-11.31	94.62	47.39	63.89	-1.18	63.12
GS/E (1)	10.0	-234.89	76.09	8.99	41.09	10.70	93.79
GS/E (2)	11.6	189.95	85.58	-9.15	43.99	-8.49	89.69
Thick disk	25.4	2.13	69.98	183.15	48.36	1.75	54.21

Table 4: XD-GMM component weights and kinematics for the low- $\alpha$  sequence. Velocities are in  $\text{km s}^{-1}$ . Weights are the fractional contribution of each component.

## 5.6 Contrasting the high and low $\alpha$ GMMs

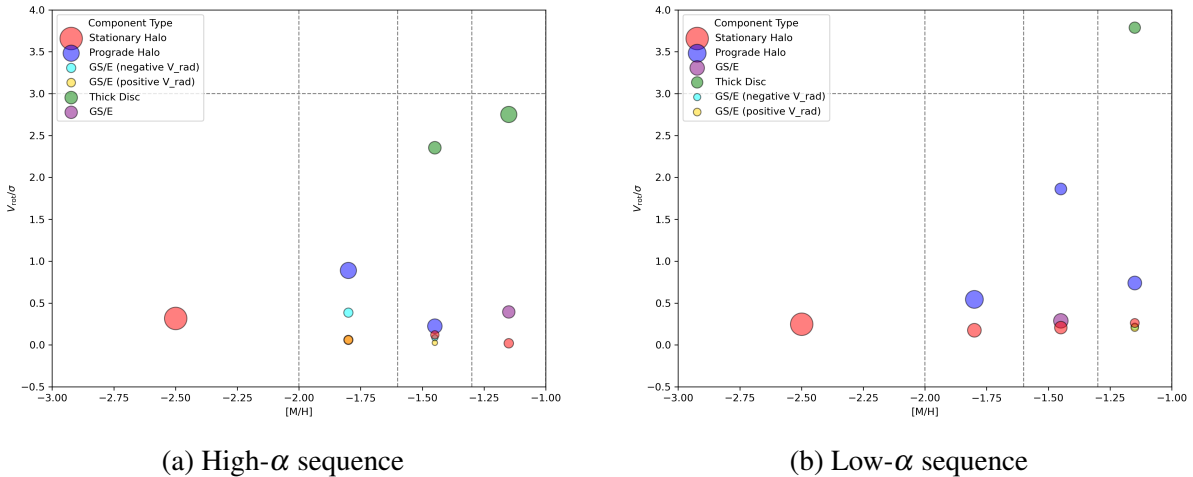


Figure 15: Ratio of the mean rotational velocity to azimuthal velocity dispersion,  $V_{\text{rot}}/\sigma_\phi$ , for individual GMM components in each metallicity bin. Larger circles represent more dominant components. Colours correspond to those in Figures 13 and 14. This is created in the same way as Figure 7.

In the very-metal-poor bin (VMP;  $[\text{M}/\text{H}] < -2$ ), both high- and low- $\alpha$  populations are dominated by a single, isotropic, non-rotating halo component. The similarity in  $V_{\text{rot}}/\sigma_\phi$  across both tracks implies that  $\alpha$ -abundance has little influence on halo structure at these low metallicities.

At intermediate metallicities (IMP;  $-2.0 < [\text{M}/\text{H}] < -1.6$ ), the low- $\alpha$  sample separates into stationary and prograde halo components, while the high- $\alpha$  fit includes two radially biased components with limited rotation. These are likely artefacts of overfitting or contamination by misclassified low- $\alpha$  stars.

In the MP1 bin ( $-1.6 < [\text{M}/\text{H}] < -1.3$ ), a thick disk component emerges in the high- $\alpha$  population, showing moderate  $V_{\text{rot}}/\sigma_{\phi}$ , indicative of in-situ disk formation. Meanwhile, the low- $\alpha$  population develops a GS/E-like halo structure, supporting a scenario where the GS/E merger occurred around the onset of high- $\alpha$  disk formation [Helmi et al., 2018].

In the most metal-rich bin (MP2;  $-1.3 < [\text{M}/\text{H}] < -1.0$ ), both sequences display prominent disk components. The high- $\alpha$  disk is kinematically hotter and more massive, while the low- $\alpha$  disk shows a sharp increase in  $V_{\text{rot}}/\sigma_{\phi}$ , consistent with a dynamically colder, thin-disk-like population. The abrupt rise suggests that thin disk formation may have occurred rapidly in the low- $\alpha$  sequence, in contrast to the more gradual buildup in the high- $\alpha$  case.

## 6 Discussion

### 6.1 Reproducability of Zhang et al. [2024]

The GMM decomposition presented in this report successfully reproduces the same structural features reported by Zhang et al. [2024] by selecting the minimum BIC score for each bin. However, there are several differences in our results worth highlighting.

At the very metal-poor end, our model recovers a nearly even split between stationary and prograde halo components, in contrast to the more dominant non-rotating halo found by Zhang et al. [2024]. Although the underlying stellar samples are largely the same, this discrepancy likely reflects the sensitivity of the GMM to initialisation and the precise kinematic distribution of stars in this low-metallicity regime, where substructure is subtle and overlapping. Notably, the kinematics of the prograde component in our fit are consistent with those reported for Aurora [Belokurov and Kravtsov, 2022], suggesting it may correspond to an early, slightly rotating in-situ population.

In the intermediate metallicity regime ( $-2.0 < [\text{M}/\text{H}] < -1.6$ ), both studies show GS/E-like signatures. The agreement in component structure is remarkably consistent, though our fit assigns slightly more weight to the GS/E substructures. Interestingly, our GS/E components appear with clearer symmetry in radial velocity, which may indicate differences in how the GMM partitions stars with highly eccentric orbits. The recovery of these features in both analyses suggests an ancient radial merger consistent with GS/E [Belokurov et al., 2020].

In the disk onset bin ( $-1.6 < [\text{M}/\text{H}] < -1.3$ ), we find a somewhat higher fraction of thick-disk stars than Zhang et al. [2024], along with slightly lower rotational velocities. This could be due to small variations in how the GMM distinguishes between disk-like and halo-like stars in the transition regime. Despite this, both studies detect a clear emergence of a warm, rotating in-situ component, consistent with the kinematics of a thick disk.

By  $[\text{M}/\text{H}] > -1.3$ , the thick disk becomes a dominant structure in our analysis and that performed by Zhang et al. [2024], almost surpassing the weight of the prograde halo.

In summary, while small discrepancies exist, particularly in the balance between halo and prograde components at low metallicity, there is an overall agreement in results.

We note that we do not attempt to reproduce the action-space analysis of Zhang et al. [2024] in this report. This decision reflects the fact that our analysis focuses on the use of the XD-GMM algorithm, and because of our understanding that orbital actions do not generally follow Gaussian distributions. Unlike velocity space, which can often be approximated as locally

Gaussian for distinct stellar populations, action space retains strong imprints of past dynamical processes (e.g. mergers, phase-mixing, resonances) that result in highly non-Gaussian, often multimodal structures.

## 6.2 Expansion of Viswanathan et al. [2024]

We extended the XD-GMM analysis to the high and low  $\alpha$  sequences identified by Viswanathan et al. [2024]. Rather than assuming two Gaussian components as in Viswanathan et al. [2024], we fit a Gaussian mixture model with varying numbers of components in each metallicity bin for both sequences. For each case, the optimal number of components was selected based on the minimum BIC score. This allows us to capture the full complexity of the kinematic structure in both sequences, including the presence of multiple halo components and the emergence of thick disk structures at different metallicities.

We were successfully able to reproduce the figures and data preparation described in Viswanathan et al. [2024], as shown in the plots of Section 5.2.

As outlined in Section 5.1, we expected structural differences between the high- and low- $\alpha$  sequences to emerge in the GMM fits. These expectations were largely met: the high- $\alpha$  stars exhibited a clear transition towards a rotationally supported disk at earlier metallicities, while the low- $\alpha$  stars remained halo-dominated until higher metallicities.

One of the more unexpected outcomes of this analysis is the identification of GS/E components within the high- $\alpha$  sequence, despite the GS/E progenitor being associated with a slow star formation history that should result in an  $\alpha$ -poor population. This is likely due to contamination from low signal-to-noise abundance measurements, or challenges in separating overlapping kinematic substructures when using GMMs. In future work, it would be helpful to consider how abundance uncertainties, particularly at low metallicities, may affect the classification of stars. Additionally, as seen in Figure 9, there appears to be a number of low- $\alpha$  stars at  $[M/H] \sim -2.5$  with  $[\alpha/M] \sim 0.1$ . It remains unclear whether this population is real or the result of measurement uncertainties, and it would benefit from further investigation.

## 6.3 Selection Effects

This part of the discussion closely follows the treatment of selection effects in Zhang et al. [2024]. As in their study, our application of quality cuts, such as removing stars with high extinction or low Galactic latitude, and enforcing a strict parallax quality threshold, introduces a non-trivial selection function that affects the relative detectability of different Galactic components.

In particular, the Galactic latitude cut removes many stars near the disk midplane, where the thin disk is most prominent. While relaxing this cut does lead to the identification of a colder, lower-dispersion disk component in the low- $\alpha$  sequence at higher metallicities, this component is not considered in our analysis. Our focus is on characterising the onset of disk like kinematics across metallicity in both chemical sequences, rather than describing the well established thin disk. Including low latitude stars would bias the sample toward the disk population, introduce uncertainties in the metallicity estimates, since Gaia XP abundances are known to be less reliable in regions of high extinction, and obscure the halo to disk transition that is central to this investigation.

It is important to emphasise that the component weights derived in this work reflect the properties of our selected sample and should not be generalised to the full Galaxy without modelling the underlying selection function.

## 6.4 Limitations of GMM

Although this part of the discussion mirrors that of [Zhang et al. \[2024\]](#), it is worth reiterating that the Gaussian mixture model approach has several limitations. Gaussian mixtures impose symmetric, ellipsoidal structures in velocity space, which is an oversimplification of the true distribution function of Galactic populations. For instance, the velocity distribution of the thin disk is considered to be non Gaussian due to features such as asymmetric drift [[Li et al., 2024](#)], while the GS/E debris has been shown to display bimodal structure in the radial velocity component [[Lancaster et al., 2019](#), [Necib et al., 2019](#)]. In addition, resonant interactions with the Galactic bar may introduce asymmetric and non Gaussian features in the velocity distributions [e.g. [Dillamore et al., 2023](#)].

Following [Zhang et al. \[2024\]](#), we therefore restricted our GMM analysis to the range  $-3 < [\text{M}/\text{H}] < -1$ , where the thin disk contribution is minimal. At higher metallicities, the GMM attempts to describe the sharp kinematic features of the thin disk using multiple Gaussians, which are not physically meaningful. While more flexible models based on physically motivated distribution functions could better capture these complexities [e.g. [Binney, 2010](#)], they require significantly more computational effort and are beyond the scope of the aims of both this report and that of [Zhang et al. \[2024\]](#).

Another known limitation of GMMs is their reduced sensitivity to small subpopulations. Like [Zhang et al. \[2024\]](#), we find little evidence for a significant disk like component at low metallicities, but this absence should be interpreted with caution.

## 6.5 Recommendations and Next Steps

To better the physical picture exposed by the XD-GMM analysis, the first priority is to replace descriptive Gaussian mixtures with fully dynamical models. Action-based or distribution-function fitting with packages such as ROADMAPPING or AGAMA can recover asymmetric wings and resonant features, tying each kinematic component directly to the Galactic potential. In parallel, cross-matching our *Gaia* sample with high-resolution spectra from APOGEE, GALAH, and the forthcoming WEAVE and 4MOST surveys will tighten the  $\alpha$ -abundance uncertainties to a few hundredths of a dex, removing the present overlap between the high- and low- $\alpha$  tracks. Once those cleaner chemical labels are in place, a forward model of *Gaia*'s selection function—encompassing its magnitude limits, colour cuts, and sky-coverage completeness—can translate the fitted mixture weights into *unbiased* stellar-mass fractions for each kinematic component. Plotting these bias-corrected masses against look-back time, or metallicity, produces a star-formation-efficiency (SFE) curve: a quantitative record of how efficiently gas was converted into stars in the thick and thin disks at every epoch. Because the underlying masses are corrected for observational selection effects, this procedure could deliver reliable SFE curves for both disks, giving a direct benchmark for galaxy-formation models.

With tighter chemical constraints in hand, the empirical  $[\text{M}/\text{H}]-\alpha$  thresholds can be folded into Milky-Way zoom simulations such as AURIGA and FIRE-2, allowing the thick- and thin-disk analogues to be tracked self-consistently through cosmic time and yielding synthetic data cubes tailored to forthcoming observatories.

Near-infrared imaging with *JWST* is the natural next step: red-giant stars—dominant in the low-surface-brightness outskirts of spirals—peak in the NIR and are only weakly affected by dust. *JWST* therefore resolves individual giants well beyond the Local Group, and NIRSpec simultaneously records the CO, CN and Fe-peak features required for accurate [M/H] and  $[\alpha/\text{Fe}]$  measurements for each star [Jakobsen et al., 2022].

The Rubin Observatory’s Legacy Survey of Space and Time will deliver the complementary view. A decade of deep, multi-epoch imaging will map whole galactic disks to very faint limits, provide sub-mas  $\text{yr}^{-1}$  proper motions for bright giants, and trace stellar-density variations at per-cent fidelity [Ivezic et al., 2019]. Combined, *JWST* spectroscopy and LSST astrometry will furnish full six-dimensional phase-space coordinates plus detailed chemistry for resolved giants in dozens of nearby spirals.

Once those data arrive, the XD-GMM method can be applied wholesale to external galaxies, decomposing their velocity fields into halo, thick-disk and thin-disk components and measuring the metallicity- $\alpha$  spin-up thresholds in each system. What is now a single-galaxy case study will become a statistically robust, cross-galaxy experiment that tests the Milky Way’s two-phase disk-assembly scenario against a much broader population of spirals.

## 7 Conclusion

We have successfully reproduced the XD-GMM work of Zhang et al. [2024] with *Gaia* DR3 red giants and confirmed that no rotation-supported disk exists below  $[\text{M}/\text{H}] \simeq -2$ , while ordered rotation appears at  $[\text{M}/\text{H}] \simeq -1.6$ . Adding XP-based  $\alpha$  abundances [Li et al., 2023] and the high/low- $\alpha$  split of Viswanathan et al. [2024] reveals a chemically tagged, two-phase timeline: high- $\alpha$  stars spin up first and build the thick disk, whereas low- $\alpha$  stars remain halo-like until  $[\text{M}/\text{H}] \approx -1.3$ , signalling the birth of a less-dispersed disk, signalling thin-disk onset. These thresholds tighten earlier, purely metallicity pictures of disk growth and provide quantitative anchors for dynamical modelling, chemical-tagging surveys and simulation work.

The path forward is therefore clear: adopt action-based distribution-function fitting to replace descriptive Gaussians, sharpen the  $\alpha$  scale with forthcoming high-resolution spectroscopy, correct mixture weights with an explicit *Gaia* selection function, and inject the resulting [M/H]- $\alpha$  thresholds into AURIGA and FIRE-2 zoom simulations. Synthetic *JWST* and LSST data built from those simulations will put the Milky Way’s two-phase disk-assembly timeline to its first rigorous, galaxy-to-galaxy test.

## References

- D. An and T. C. Beers. A blueprint for the milky way’s stellar populations: The power of large photometric and astrometric surveys. *The Astrophysical Journal*, 897(1):39, July 2020. doi: 10.3847/1538-4357/ab8d39. URL <https://ui.adsabs.harvard.edu/abs/2020ApJ...897...39A>.
- F. Anders, P. Gispert, B. Ratcliffe, C. Chiappini, I. Minchev, S. Nepal, A. B. A. Queiroz, J. A. S. Amarante, T. Antoja, G. Casali, L. Casamiquela, A. Khalatyan, A. Miglio, H. Perottoni, and M. Schultheis. Spectroscopic age estimates for apogee red-giant stars: Precise spatial and kinematic trends with age in the galactic disc. *Astronomy and Astrophysics*, 678: A158, Oct. 2023. ISSN 1432-0746. doi: 10.1051/0004-6361/202346666. URL <http://dx.doi.org/10.1051/0004-6361/202346666>.
- R. Andrae, H.-W. Rix, and V. Chandra. Robust data-driven metallicities for 175 million stars from gaia xp spectra. *The Astrophysical Journal Supplement Series*, 267(1):8, jul 2023. doi: 10.3847/1538-4365/acd53e. URL <https://dx.doi.org/10.3847/1538-4365/acd53e>.
- A. Arentsen, E. Starkenburg, N. F. Martin, D. S. Aguado, D. B. Zucker, C. Allende Prieto, V. Hill, K. A. Venn, R. G. Carlberg, J. I. González Hernández, L. I. Mashonkina, J. F. Navarro, R. Sánchez-Janssen, M. Schultheis, G. F. Thomas, K. Youakim, G. F. Lewis, J. D. Simpson, Z. Wan, R. E. Cohen, D. Geisler, and J. E. O’Connell. The pristine inner galaxy survey (pigs) ii: Uncovering the most metal-poor populations in the inner milky way. *Monthly Notices of the Royal Astronomical Society*, 496(4):4964–4978, July 2020a. ISSN 1365-2966. doi: 10.1093/mnras/staa1661. URL <http://dx.doi.org/10.1093/mnras/staa1661>.
- A. Arentsen, E. Starkenburg, N. F. Martin, V. Hill, R. Ibata, A. Kunder, M. Schultheis, K. A. Venn, D. B. Zucker, D. Aguado, R. Carlberg, J. I. González Hernández, C. Lardo, N. Longeard, K. Malhan, J. F. Navarro, R. Sánchez-Janssen, F. Sestito, G. Thomas, K. Youakim, G. F. Lewis, J. D. Simpson, and Z. Wan. The pristine inner galaxy survey (pigs) i: Tracing the kinematics of metal-poor stars in the galactic bulge. *Monthly Notices of the Royal Astronomical Society*, 491(1):L11–L16, January 2020b. doi: 10.1093/mnrasl/slz156. URL <https://ui.adsabs.harvard.edu/abs/2020MNRAS..491L..11A>.
- C. A. L. Bailer-Jones, J. Rybizki, M. Fouesneau, M. Demleitner, and R. Andrae. VizieR Online Data Catalog: Distances to 1.47 billion stars in Gaia EDR3 (Bailer-Jones+, 2021). art. I/352, Feb. 2021.
- V. Belokurov and A. Kravtsov. From dawn till disc: Milky way’s turbulent youth revealed by the apogee+gaia data. *Monthly Notices of the Royal Astronomical Society*, 514(1):689–714, May 2022. ISSN 1365-2966. doi: 10.1093/mnras/stac1267. URL <http://dx.doi.org/10.1093/mnras/stac1267>.
- V. Belokurov, D. Erkal, N. W. Evans, S. E. Koposov, and A. J. Deason. Co-formation of the disc and the stellar halo. *Monthly Notices of the Royal Astronomical Society*, 478(1):611–619, June 2018. ISSN 1365-2966. doi: 10.1093/mnras/sty982. URL <http://dx.doi.org/10.1093/mnras/sty982>.
- V. Belokurov, J. L. Sanders, A. Fattahi, M. C. Smith, A. J. Deason, N. W. Evans, and R. J. J. Grand. The biggest splash. *Monthly Notices of the Royal Astronomical Society*, 494(3): 3880–3898, Apr. 2020. ISSN 1365-2966. doi: 10.1093/mnras/staa876. URL <http://dx.doi.org/10.1093/mnras/staa876>.

- J. Binney. Distribution functions for the milky way. *Monthly Notices of the Royal Astronomical Society*, 401(4):2318–2330, Feb. 2010. ISSN 1365-2966. doi: 10.1111/j.1365-2966.2009.15845.x. URL <http://dx.doi.org/10.1111/j.1365-2966.2009.15845.x>.
- S. A. Bird, X.-X. Xue, C. Liu, J. Shen, C. Flynn, C. Yang, G. Zhao, and H.-J. Tian. Constraints on the assembly history of the milky way’s smooth, diffuse stellar halo from the metallicity-dependent, radially dominated velocity anisotropy profiles probed with k giants and bhb stars using lamost, sdss/segue, and gaia. *The Astrophysical Journal*, 919(1):66, Sept. 2021. ISSN 1538-4357. doi: 10.3847/1538-4357/abfa9e. URL <http://dx.doi.org/10.3847/1538-4357/abfa9e>.
- J. Bland-Hawthorn and O. Gerhard. The galaxy in context: Structural, kinematic, and integrated properties. *Annual Review of Astronomy and Astrophysics*, 54(1):529–596, Sept. 2016. ISSN 1545-4282. doi: 10.1146/annurev-astro-081915-023441. URL <http://dx.doi.org/10.1146/annurev-astro-081915-023441>.
- J. Bovy, D. W. Hogg, and S. T. Roweis. Extreme deconvolution: Inferring complete distribution functions from noisy, heterogeneous and incomplete observations. *The Annals of Applied Statistics*, 5(2B), June 2011. ISSN 1932-6157. doi: 10.1214/10-aos439. URL <http://dx.doi.org/10.1214/10-aos439>.
- J. S. Bullock and M. Boylan-Kolchin. Small-scale challenges to the lambda cdm paradigm. *Annual Review of Astronomy and Astrophysics*, 55(1):343–387, Aug. 2017. ISSN 1545-4282. doi: 10.1146/annurev-astro-091916-055313. URL <http://dx.doi.org/10.1146/annurev-astro-091916-055313>.
- D. Carollo, M. Chiba, M. Ishigaki, K. Freeman, T. C. Beers, Y. S. Lee, P. Tissera, C. Battistini, and F. Primas. Evidence for the third stellar population in the milky way’s disk. *The Astrophysical Journal*, 887(1):22, December 2019. doi: 10.3847/1538-4357/ab517c. URL <https://ui.adsabs.harvard.edu/abs/2019ApJ...887...22C>.
- V. Chandra, V. A. Semenov, H.-W. Rix, C. Conroy, A. Bonaca, R. P. Naidu, R. Andrae, J. Li, and L. Hernquist. The three-phase evolution of the milky way. *The Astrophysical Journal*, 972(1):112, Aug. 2024. ISSN 1538-4357. doi: 10.3847/1538-4357/ad5b60. URL <http://dx.doi.org/10.3847/1538-4357/ad5b60>.
- M. Chiba and T. C. Beers. Kinematics of metal-poor stars in the galaxy. iii. formation of the stellar halo and thick disk as revealed from a large sample of nonkinematically selected stars. *The Astronomical Journal*, 119(6):2843–2865, June 2000. ISSN 0004-6256. doi: 10.1086/301409. URL <http://dx.doi.org/10.1086/301409>.
- G. Cordoni, G. S. Da Costa, D. Yong, A. D. Mackey, A. F. Marino, S. Monty, T. Nordlander, J. E. Norris, M. Asplund, M. S. Bessell, A. R. Casey, A. Frebel, K. Lind, S. J. Murphy, B. P. Schmidt, X. D. Gao, T. Xylakis-Dornbusch, A. M. Amarsi, and A. P. Milone. Exploring the galaxy’s halo and very metal-weak thick disc with skymapper and gaia dr2. *Monthly Notices of the Royal Astronomical Society*, 503(2):2539–2561, Nov. 2020. ISSN 1365-2966. doi: 10.1093/mnras/staa3417. URL <http://dx.doi.org/10.1093/mnras/staa3417>.
- P. Di Matteo, M. Haywood, M. D. Lehnert, D. Katz, S. Khoperskov, O. N. Snaith, A. Gomez, and N. Robichon. The milky way has no in-situ halo other than the heated thick disc: Composition of the stellar halo and age-dating the last significant merger with gaia dr2 and apogee.

*Astronomy & Astrophysics*, 632:A4, Nov. 2019. ISSN 1432-0746. doi: 10.1051/0004-6361/201834929. URL <http://dx.doi.org/10.1051/0004-6361/201834929>.

- A. M. Dillamore, V. Belokurov, N. W. Evans, and E. Y. Davies. Stellar halo substructure generated by bar resonances. *Monthly Notices of the Royal Astronomical Society*, 524(3): 3596–3608, July 2023. ISSN 1365-2966. doi: 10.1093/mnras/stad2136. URL <http://dx.doi.org/10.1093/mnras/stad2136>.
- Gaia Collaboration, A. Vallenari, A. G. A. Brown, et al. Gaia data release 3: Summary of the content and survey properties. *Astronomy & Astrophysics*, 674:A1, 2023. doi: 10.1051/0004-6361/202243940.
- C. Gallart, E. J. Bernard, C. B. Brook, T. Ruiz-Lara, S. Cassisi, V. Hill, and M. Monelli. Uncovering the birth of the milky way through accurate stellar ages with gaia. *Nature Astronomy*, 3(10):932–939, July 2019. ISSN 2397-3366. doi: 10.1038/s41550-019-0829-5. URL <http://dx.doi.org/10.1038/s41550-019-0829-5>.
- D. F. Gray. *The Observation and Analysis of Stellar Photospheres*. Cambridge University Press, 2005.
- G. M. Green. dustmaps: A python interface for maps of interstellar dust. *Journal of Open Source Software*, 3(26):695, 2018. doi: 10.21105/joss.00695. URL <https://doi.org/10.21105/joss.00695>.
- A. B. Gurvich, J. Stern, C.-A. Faucher-Giguère, P. F. Hopkins, A. Wetzel, J. Moreno, C. C. Hayward, A. J. Richings, and Z. Hafen. Rapid disc settling and the transition from bursty to steady star formation in milky way-mass galaxies. *Monthly Notices of the Royal Astronomical Society*, 519(2):2598–2614, February 2023. doi: 10.1093/mnras/stac3712. URL <https://ui.adsabs.harvard.edu/abs/2023MNRAS.519.2598G>.
- M. Haywood, P. Di Matteo, M. D. Lehnert, D. Katz, and A. Gómez. The age structure of stellar populations in the solar vicinity: Clues of a two-phase formation history of the milky way disk. *Astronomy and Astrophysics*, 560:A109, Dec. 2013. ISSN 1432-0746. doi: 10.1051/0004-6361/201321397. URL <http://dx.doi.org/10.1051/0004-6361/201321397>.
- A. Helmi. Streams, substructures, and the early history of the milky way. *Annual Review of Astronomy and Astrophysics*, 58(1):205–256, Aug. 2020. ISSN 1545-4282. doi: 10.1146/annurev-astro-032620-021917. URL <http://dx.doi.org/10.1146/annurev-astro-032620-021917>.
- A. Helmi, C. Babusiaux, H. H. Koppelman, D. Massari, J. Veljanoski, and A. G. A. Brown. The merger that led to the formation of the milky way’s inner stellar halo and thick disk. *Nature*, 563(7729):85–88, Oct. 2018. ISSN 1476-4687. doi: 10.1038/s41586-018-0625-x. URL <http://dx.doi.org/10.1038/s41586-018-0625-x>.
- V. Ivezić, S. M. Kahn, J. A. Tyson, B. Abel, E. Acosta, R. Allsman, D. Alonso, Y. AlSayyad, S. F. Anderson, and J. Andrew. Lsst: From science drivers to reference design and anticipated data products. *The Astrophysical Journal*, 873(2):111, Mar. 2019. doi: 10.3847/1538-4357/ab042c. URL <https://doi.org/10.3847/1538-4357/ab042c>.
- P. Jakobsen, P. Ferruit, C. Alves de Oliveira, S. Arribas, G. Bagnasco, R. Barho, T. L. Beck, S. Birkmann, T. Böker, A. J. Bunker, S. Charlot, P. de Jong, G. de Marchi, R. Ehrenwinkler,

- M. Falcolini, R. Fels, M. Franx, D. Franz, M. Funke, G. Giardino, X. Gnata, W. Holota, K. Honnen, P. L. Jensen, M. Jentsch, T. Johnson, D. Jollet, H. Karl, G. Kling, J. Köhler, M.-G. Kolm, N. Kumari, M. E. Lander, R. Lemke, M. López-Caniego, N. Lützgendorf, R. Maiolino, E. Manjavacas, A. Marston, M. Maschmann, R. Maurer, B. Messerschmidt, S. H. Moseley, P. Mosner, D. B. Mott, J. Muzerolle, N. Pirzkal, J.-F. Pittet, A. Plitzke, W. Posselt, B. Rapp, B. J. Rauscher, T. Rawle, H.-W. Rix, A. Rödel, P. Rumler, E. Sabbi, J.-C. Salvignol, T. Schmid, M. Sirianni, C. Smith, P. Strada, M. te Plate, J. Valenti, T. Wettemann, T. Wiehe, M. Wiesmayer, C. J. Willott, R. Wright, P. Zeidler, and C. Zincke. The near-infrared spectrograph (nirspec) on the james webbspace telescope: I. overview of the instrument and its capabilities. *Astronomy and Astrophysics*, 661:A80, May 2022. ISSN 1432-0746. doi: 10.1051/0004-6361/202142663. URL <http://dx.doi.org/10.1051/0004-6361/202142663>.
- L. Lancaster, S. E. Koposov, V. Belokurov, N. W. Evans, and A. J. Deason. The halo's ancient metal-rich progenitor revealed with bhb stars. *Monthly Notices of the Royal Astronomical Society*, 486(1):378–389, Mar. 2019. ISSN 1365-2966. doi: 10.1093/mnras/stz853. URL <http://dx.doi.org/10.1093/mnras/stz853>.
- H. W. Leung and J. Bovy. Deep learning of multi-element abundances from high-resolution spectroscopic data. *Monthly Notices of the Royal Astronomical Society*, 483(3):3255–3277, 2019.
- J. Li, K. W. K. Wong, D. W. Hogg, H.-W. Rix, and V. Chandra. Asgap: Augmented stellar parameters and abundances for 23 million rgb stars from gaia xp low-resolution spectra, 2023. URL <https://arxiv.org/abs/2309.14294>.
- X. Li, P. Yang, H.-F. Wang, Q. Li, Y.-P. Luo, Z.-Q. Luo, and G.-Y. Wang. Asymmetric drift map of the milky way disk populations between 8 -16 kpc with lamost and gaia datasets. *The Open Journal of Astrophysics*, 7, May 2024. ISSN 2565-6120. doi: 10.33232/001c.117594. URL <http://dx.doi.org/10.33232/001c.117594>.
- M. K. Mardini, A. Frebel, A. Chiti, Y. Meiron, K. V. Brauer, and X. Ou. The atari disk, a metal-poor stellar population in the disk system of the milky way. *The Astrophysical Journal*, 936(1):78, Sept. 2022. ISSN 1538-4357. doi: 10.3847/1538-4357/ac8102. URL <http://dx.doi.org/10.3847/1538-4357/ac8102>.
- P. J. McMillan. The mass distribution and gravitational potential of the milky way. *Monthly Notices of the Royal Astronomical Society*, 465(1):76–94, Oct. 2016. ISSN 1365-2966. doi: 10.1093/mnras/stw2759. URL <http://dx.doi.org/10.1093/mnras/stw2759>.
- P. Melchior and A. Goulding. Filling the gaps: Gaussian mixture models from noisy, truncated or incomplete samples. *Astronomy and Computing*, 25, 11 2016. doi: 10.1016/j.ascom.2018.09.013.
- L. Necib, M. Lisanti, and V. Belokurov. Inferred evidence for dark matter kinematic substructure with sdss–gaia. *The Astrophysical Journal*, 874(1):3, mar 2019. doi: 10.3847/1538-4357/ab095b. URL <https://dx.doi.org/10.3847/1538-4357/ab095b>.
- B. Nordström, M. Mayor, J. Andersen, J. Holmberg, F. Pont, B. R. Jørgensen, E. H. Olsen, S. Udry, and N. Mowlavi. The geneva-copenhagen survey of the solar neighbourhood: Ages, metallicities, and kinematic properties of  $\sim$ 14 000 f and g dwarfs. *Astronomy and amp;*

- Astrophysics*, 418(3):989–1019, Apr. 2004. ISSN 1432-0746. doi: 10.1051/0004-6361:20035959. URL <http://dx.doi.org/10.1051/0004-6361:20035959>.
- J. Norris, M. S. Bessell, and A. J. Pickles. Population studies. i. the bidelman-macconnell “weak-metal” stars. *The Astrophysical Journal Supplement Series*, 58:463–492, July 1985. doi: 10.1086/191049. URL <https://ui.adsabs.harvard.edu/abs/1985ApJS...58..463N>.
- A. B. Pace. The Local Volume Database: a library of the observed properties of nearby dwarf galaxies and star clusters. *arXiv e-prints*, art. arXiv:2411.07424, Nov. 2024. doi: 10.48550/arXiv.2411.07424.
- C. W. Purcell, J. S. Bullock, and A. R. Zentner. Shredded galaxies as the source of diffuse intrahalo light on varying scales. *The Astrophysical Journal*, 666(1):20–33, Sept. 2007. ISSN 1538-4357. doi: 10.1086/519787. URL <http://dx.doi.org/10.1086/519787>.
- B. Ratcliffe, I. Minchev, G. Cescutti, E. Spitoni, H. Jönsson, F. Anders, A. Queiroz, and M. Steinmetz. Chemical clocks and their time zones: understanding the [s/mg]–age relation with birth radii, 2023. URL <https://arxiv.org/abs/2307.11159>.
- H.-W. Rix, V. Chandra, R. Andrae, A. M. Price-Whelan, D. H. Weinberg, C. Conroy, M. Fouesneau, D. W. Hogg, F. De Angeli, R. P. Naidu, M. Xiang, and D. Ruz-Mieres. The poor old heart of the milky way. *The Astrophysical Journal*, 941(1):45, Dec. 2022. ISSN 1538-4357. doi: 10.3847/1538-4357/ac9e01. URL <http://dx.doi.org/10.3847/1538-4357/ac9e01>.
- I. B. Santistevan, A. Wetzel, R. E. Sanderson, K. El-Badry, J. Samuel, and C.-A. Faucher-Giguère. The origin of metal-poor stars on prograde disc orbits in fire simulations of milky way-mass galaxies. *Monthly Notices of the Royal Astronomical Society*, 505(1):921–938, July 2021. doi: 10.1093/mnras/stab1345. URL <https://ui.adsabs.harvard.edu/abs/2021MNRAS.505..921S>.
- G. Schwarz. Estimating the dimension of a model. *The Annals of Statistics*, 6(2):461–464, 1978. ISSN 00905364, 21688966. URL <http://www.jstor.org/stable/2958889>.
- R. Schönrich, J. Binney, and W. Dehnen. Local kinematics and the local standard of rest. *Monthly Notices of the Royal Astronomical Society*, 403(4):1829–1833, Apr. 2010. ISSN 1365-2966. doi: 10.1111/j.1365-2966.2010.16253.x. URL <http://dx.doi.org/10.1111/j.1365-2966.2010.16253.x>.
- F. Sestito, N. Martin, and E. Starkenburg. Tracing the formation of the milky way through ultra metal-poor stars. In *The Gaia Universe*, page 47, Apr. 2019. doi: 10.5281/zenodo.3236051.
- F. Sestito, T. Buck, E. Starkenburg, N. F. Martin, J. F. Navarro, K. A. Venn, A. Obreja, P. Jablonka, and A. V. Macciò. Exploring the origin of low-metallicity stars in milky-way-like galaxies with the nihao-uhd simulations. *Monthly Notices of the Royal Astronomical Society*, 500(3):3750–3762, Nov. 2020. ISSN 1365-2966. doi: 10.1093/mnras/staa3479. URL <http://dx.doi.org/10.1093/mnras/staa3479>.
- V. Springel, J. Wang, M. Vogelsberger, A. Ludlow, A. Jenkins, A. Helmi, J. F. Navarro, C. S. Frenk, and S. D. M. White. The aquarius project: the subhaloes of galactic haloes. *Monthly Notices of the Royal Astronomical Society*, 391(4):1685–1711, Dec. 2008. ISSN 1365-

2966. doi: 10.1111/j.1365-2966.2008.14066.x. URL <http://dx.doi.org/10.1111/j.1365-2966.2008.14066.x>.
- R. Tkachenko, K. Vieira, A. Lutsenko, V. Korchagin, and G. Carraro. Determining the scale length and height of the milky way’s thick disc using rr lyrae. *Universe*, 11(4):132, apr 2025. doi: 10.3390/universe11040132. URL <http://dx.doi.org/10.3390/universe11040132>.
- K. A. Venn, C. L. Kielty, F. Sestito, E. Starkenburg, N. Martin, D. S. Aguado, A. Arentsen, P. Bonifacio, E. Caffau, V. Hill, P. Jablonka, C. Lardo, L. Mashonkina, J. F. Navarro, C. Sneden, G. Thomas, K. Youakim, J. I. González-Hernández, R. S. Janssen, R. Carlberg, and K. Malhan. The pristine survey - ix. cfht espadons spectroscopic analysis of 115 bright metal-poor candidate stars. *Monthly Notices of the Royal Astronomical Society*, 492(3):3241–3262, Mar. 2020. doi: 10.1093/mnras/stz3546.
- A. Viswanathan, D. Horta, A. M. Price-Whelan, and E. Starkenburg. A slow spin to win – the gradual evolution of the proto-galaxy to the old disc, 2024. URL <https://arxiv.org/abs/2411.12165>.
- H. Zhang, A. Ardern-Arentsen, and V. Belokurov. On the existence of a very metal-poor disc in the milky way, 2024. URL <https://arxiv.org/abs/2311.09294>.

## Declaration of Use of AI Tools

I declare that all ideas, methods, and approaches used in this project were conceived and developed independently through my own research, understanding and engagement with lecture and supervision material. The work presented here is entirely my own.

The following AI tools were used for support purposes:

- **ChatGPT:** Used to refine code snippets, assist with LaTeX formatting, assist with documentation, and improve the clarity and structure. All content generated by this tool was critically evaluated and adapted.
- **GitHub Copilot:** Used to suggest coding snippets and assist the implementation of functions. All suggested code was reviewed, modified, and tested.